

Planck intermediate results. XIX. An overview of the polarized thermal emission from Galactic dust

Planck Collaboration: P. A. R. Ade⁷⁸, N. Aghanim⁵⁴, D. Alina^{83,10}, M. I. R. Alves⁵⁴, C. Armitage-Caplan⁸¹, M. Arnaud⁶⁷, D. Arzoumanian⁵⁴, M. Ashdown^{64,6}, F. Atrio-Barandela¹⁸, J. Aumont⁵⁴, C. Baccigalupi⁷⁷, A. J. Banday^{83,10}, R. B. Barreiro⁶¹, E. Battaner^{85,86}, K. Benabed^{55,82}, A. Benoit-Lévy^{24,55,82}, J.-P. Bernard^{83,10}*, M. Bersanelli^{33,47}, P. Bielewicz^{83,10,77}, J. J. Bock^{62,11}, J. R. Bond⁹, J. Borrill^{13,79}, F. R. Bouchet^{55,82}, F. Boulanger⁵⁴, A. Bracco⁵⁴, C. Burigana^{46,31}, R. C. Butler⁴⁶, J.-F. Cardoso^{68,1,55}, A. Catalano^{69,66}, A. Chamballu^{67,15,54}, R.-R. Chary⁵³, H. C. Chiang^{27,7}, P. R. Christensen^{74,36}, S. Colombi^{55,82}, L. P. L. Colombo^{23,62}, C. Combet⁶⁹, F. Couchot⁶⁵, A. Coulais⁶⁶, B. P. Crill^{62,75}, A. Curto^{6,61}, F. Cuttaia⁴⁶, L. Danese⁷⁷, R. D. Davies⁶³, R. J. Davis⁶³, P. de Bernardis³², E. M. de Gouveia Dal Pino⁶⁰, A. de Rosa⁴⁶, G. de Zotti^{43,77}, J. Delabrouille¹, F.-X. Désert⁵¹, C. Dickinson⁶³, J. M. Diego⁶¹, S. Donzelli⁴⁷, O. Doré^{62,11}, M. Douspis⁵⁴, J. Dunkley⁸¹, X. Dupac³⁹, T. A. EnBlin⁷², H. K. Eriksen⁵⁸, E. Falgarone⁶⁶, K. Ferrière^{83,10}, F. Finelli^{46,48}, O. Forni^{83,10}, M. Frailis⁴⁵, A. A. Fraisse²⁷, E. Franceschi⁴⁶, S. Galeotta⁴⁵, K. Ganga¹, T. Ghosh⁵⁴, M. Giard^{83,10}, Y. Giraud-Héraud¹, J. González-Nuevo^{61,77}, K. M. Górski^{62,87}, A. Gregorio^{34,45,50}, A. Gruppuso⁴⁶, V. Guillet⁵⁴, F. K. Hansen⁵⁸, D. L. Harrison^{57,64}, G. Helou¹¹, C. Hernández-Monteagudo^{12,72}, S. R. Hildebrandt¹¹, E. Hivon^{55,82}, M. Hobson⁶, W. A. Holmes⁶², A. Hornstrup¹⁶, K. M. Huffenberger²⁵, A. H. Jaffe⁵², T. R. Jaffe^{83,10}, W. C. Jones²⁷, M. Juvela²⁶, E. Keihänen²⁶, R. Keskitalo¹³, T. S. Kisner⁷¹, R. Kneissl^{38,8}, J. Knoche⁷², M. Kunz^{17,54,3}, H. Kurki-Suonio^{26,41}, G. Lagache⁵⁴, A. Lähteenmäki^{2,41}, J.-M. Lamarre⁶⁶, A. Lasenby^{6,64}, C. R. Lawrence⁶², J. P. Leahy⁶³, R. Leonardi³⁹, F. Levrier⁶⁶, M. Liguori³⁰, P. B. Lilje⁵⁸, M. Linden-Vørnle¹⁶, M. López-Caniego⁶¹, P. M. Lubin²⁸, J. F. Macías-Pérez⁶⁹, B. Maffei⁶³, A. M. Magalhães⁶⁰, D. Maino^{33,47}, N. Mandolesi^{46,5,31}, M. Maris⁴⁵, D. J. Marshall⁶⁷, P. G. Martin⁹, E. Martínez-González⁶¹, S. Masi³², S. Matarrese³⁰, P. Mazzotta³⁵, A. Melchiorri^{32,49}, L. Mendes³⁹, A. Mennella^{33,47}, M. Migliaccio^{57,64}, M.-A. Miville-Deschênes^{54,9}, A. Moneti⁵⁵, L. Montier^{83,10}, G. Morgante⁴⁶, D. Mortlock⁵², D. Munshi⁷⁸, J. A. Murphy⁷³, P. Naselsky^{74,36}, F. Nati³², P. Natoli^{31,4,46}, C. B. Netterfield²⁰, F. Novello⁶³, D. Novikov⁵², I. Novikov⁷⁴, C. A. Oxborrow¹⁶, L. Pagano^{32,49}, F. Pajot⁵⁴, R. Paladini⁵³, D. Paoletti^{46,48}, F. Pasian⁴⁵, T. J. Pearson^{11,53}, O. Perdereau⁶⁵, L. Perotto⁶⁹, F. Perrotta⁷⁷, F. Piacentini³², M. Piat¹, D. Pietrobon⁶², S. Plaszczynski⁶⁵, F. Poidevin²⁴, E. Pointecouteau^{83,10}, G. Polenta^{4,44}, L. Popa⁵⁶, G. W. Pratt⁶⁷, S. Prunet^{55,82}, J.-L. Puget⁵⁴, J. P. Rachen^{21,72}, W. T. Reach⁸⁴, R. Rebolo^{59,14,37}, M. Reinecke⁷², M. Remazeilles^{63,54,1}, C. Renault⁶⁹, S. Ricciardi⁴⁶, T. Riller⁷², I. Ristorcelli^{83,10}, G. Rocha^{62,11}, C. Rosset¹, G. Roudier^{1,66,62}, J. A. Rubiño-Martín^{59,37}, B. Rusholme⁵³, M. Sandri⁴⁶, G. Savini⁷⁶, D. Scott²², L. D. Spencer⁷⁸, V. Stolyarov^{6,64,80}, R. Stompor¹, R. Sudiwala⁷⁸, D. Sutton^{57,64}, A.-S. Suur-Uski^{26,41}, J.-F. Sygnet⁵⁵, J. A. Tauber⁴⁰, L. Terenzi⁴⁶, L. Toffolatti^{19,61}, M. Tomasi^{33,47}, M. Tristram⁶⁵, M. Tucci^{17,65}, G. Umata⁴², L. Valenziano⁴⁶, J. Valiviita^{26,41}, B. Van Tent⁷⁰, P. Vielva⁶¹, F. Villa⁴⁶, L. A. Wade⁶², B. D. Wandelt^{55,82,29}, A. Zacchei⁴⁵, and A. Zonca²⁸

(Affiliations can be found after the references)

Preprint online version: May 6, 2014

ABSTRACT

This paper presents the large-scale polarized sky as seen by *Planck* HFI at 353 GHz, which is the most sensitive *Planck* channel for dust polarization. We construct and analyse large-scale maps of dust polarization fraction and polarization direction, while taking account of noise bias and possible systematic effects. We find that the maximum observed dust polarization fraction is high ($p_{\max} > 18\%$), in particular in some of the intermediate dust column density ($A_V < 1$ mag) regions. There is a systematic decrease in the dust polarization fraction with increasing dust column density, and we interpret the features of this correlation in light of both radiative grain alignment predictions and fluctuations in the magnetic field orientation. We also characterize the spatial structure of the polarization angle using the angle dispersion function and find that, in nearby fields at intermediate latitudes, the polarization angle is ordered over extended areas that are separated by filamentary structures, which appear as interfaces where the magnetic field sky projection rotates abruptly without apparent variations in the dust column density. The polarization fraction is found to be anti-correlated with the dispersion of the polarization angle, implying that the variations are likely due to fluctuations in the 3D magnetic field orientation along the line of sight sampling the diffuse interstellar medium. We also compare the dust emission with the polarized synchrotron emission measured with the *Planck* LFI, with low-frequency radio data, and with Faraday rotation measurements of extragalactic sources. The two polarized components are globally similar in structure along the plane and notably in the Fan and North Polar Spur regions. A detailed comparison of these three tracers shows, however, that dust and cosmic rays generally sample different parts of the line of sight and confirms that much of the variation observed in the *Planck* data is due to the 3D structure of the magnetic field.

Key words. ISM: general – ISM: dust – ISM: magnetic fields – ISM: clouds – Submillimetre: ISM

1. Introduction

Our Galaxy is pervaded by an interstellar magnetic field of a few microgauss, which fills the entire disk and extends well into the halo. This magnetic field manifests itself in a variety of ways, including Zeeman splitting of atomic and molecular spectral lines,

Faraday rotation of polarized radio signals, synchrotron emission from relativistic electrons, and polarization of starlight and thermal dust emission. With a pressure at least comparable to those of the thermal gas and of cosmic rays, the Galactic magnetic field (GMF) plays a crucial role in the ecosystem of our Galaxy. It governs the structure and the dynamics of the interstellar medium (ISM), regulates the process of star formation, accelerates cosmic rays, channels their trajectories and helps to

* Corresponding author; email: Jean-Philippe.Bernard@irap.omp.eu.

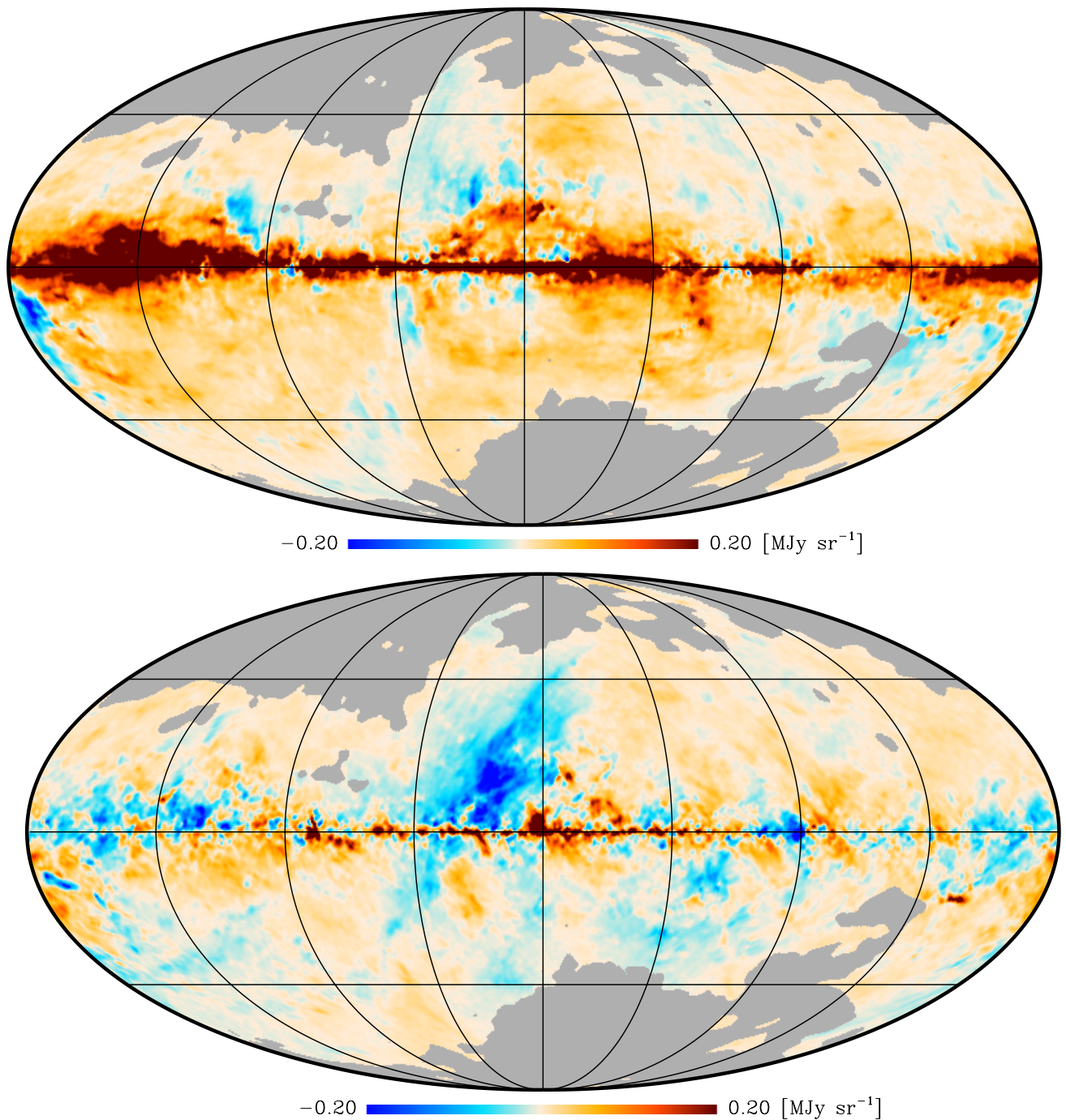


Fig. 1. *Planck* 353 GHz polarization maps at 1° resolution. *Upper*: Q Stokes parameter map. *Lower*: U Stokes parameter map. The maps are shown with the same colour scale. High values are saturated to enhance mid-latitude structures. The values shown have been bias corrected as described in Sect. 2.3. These maps, as well as those in following figures, are shown in Galactic coordinates with the galactic center in the middle and longitude increasing to the left. The data is masked as described in Sect. 2.4.

confine them to the Galaxy. In addition to a large-scale regular, or coherent, component and an isotropic random component produced by interstellar turbulence (with scales up to 100 pc; e.g., Gaensler & Johnston 1995; Haverkorn et al. 2008), the GMF also possesses an ordered random (e.g., Beck 2009; Jaffe et al. 2010), or striated random (Jansson & Farrar 2012a), component, whose orientation remains nearly constant over large scales, but whose strength and sign vary on small scales. Such fields are probably produced through compression or shearing of isotropic random

fields by the Galactic differential rotation, or at large-scale spiral arm shocks, or else by rising hot plasma bubbles.

Our knowledge and understanding of the GMF has improved considerably over the past few years, as a result of both progress in the quality (sensitivity and resolution) of radio observations and extensive modelling efforts (e.g., Sun et al. 2008; Sun & Reich 2010; Ruiz-Granados et al. 2010; Jaffe et al. 2010, 2011; Pshirkov et al. 2011; Fauvet et al. 2012; Jansson & Farrar 2012a,b; Fauvet et al. 2013). However, the existing radio obser-

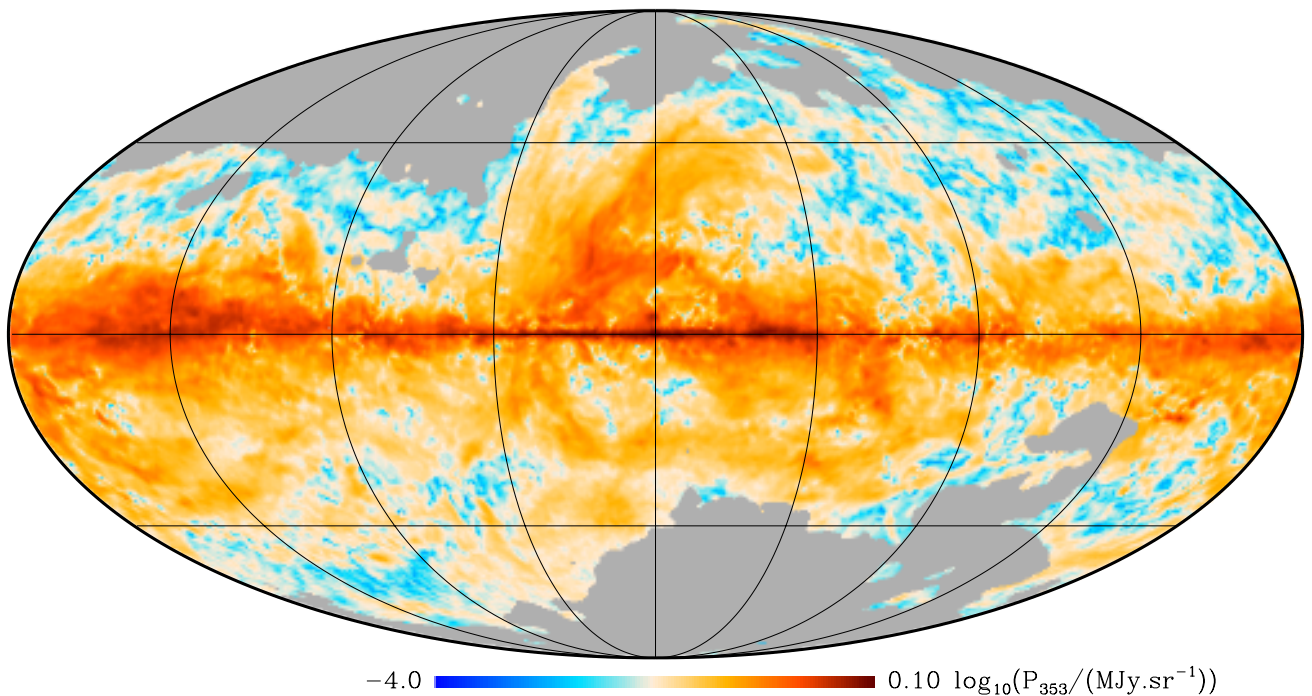


Fig. 2. *Planck* 353 GHz polarized intensity (P) map at 1° resolution in \log_{10} scale. The values shown have been bias corrected as described in Sect. 2.3. The same mask as in Fig. 1 is applied. The full sky map of the unpolarized intensity I entering the calculation of P is shown in Fig. 5.

vations have inherent limitations, as both Faraday rotation measures (RMs) and synchrotron (total and polarized) intensities are quantities integrated over the line of sight (LOS), which depend on the poorly constrained density distributions of thermal and relativistic electrons, respectively. A promising avenue to obtain a more complete and more robust picture of the GMF structure is to complement the radio data with *Planck*¹ measurements of the polarized thermal emission from interstellar dust, which is independent of the electron densities.

A glance at the *Planck* all-sky intensity maps (Planck Collaboration I 2014) reveals that, in addition to the mottled structure of the cosmic microwave background (CMB) at high Galactic latitudes, the dominant pattern is that of the emission from our Galaxy. At the lowest frequencies, from the 30 GHz to 70 GHz bands of the *Planck* Low Frequency Instrument (LFI, Bersanelli et al. 2010), synchrotron emission dominates; at the highest frequencies, from the 100 GHz to 857 GHz bands of the High Frequency Instrument (HFI, Lamarre et al. 2010), thermal emission from interstellar dust is the dominant mechanism. These foregrounds have to be understood and taken into account for detailed CMB studies, but they also provide a unique opportunity to study the Galaxy’s ISM.

In particular, the thermal dust emission is linearly polarized (e.g., Benoît et al. 2004; Vaillancourt 2007). This polarized emission overpowers any other polarized signal at the higher *Planck* frequencies (e.g., Tucci et al. 2005; Dunkley et al. 2009; Fraisse et al. 2009). In addition to hindering the detection of the sought-after, odd-parity, B -mode polarization of the CMB, the polarized

dust emission provides, in combination with the emission spectrum itself, a powerful constraint on the physical properties of the dust and on the structure of the magnetic field in the Galaxy.

The linear polarization of the thermal dust emission arises from a combination of two main factors. Firstly, a fraction of the dust grain population is non-spherical, and this gives rise to different emissivities for radiations with the electric vector parallel or orthogonal to a grain’s long axis. Secondly, the rotating grains are aligned by the interstellar magnetic field, probably with differing efficiencies depending on grain size and composition (Draine & Fraisse 2009). While the details of this process remain unclear (Lazarian 2003, 2007), there is a consensus that the angular momentum of a grain spun up by photon-grain interactions (Dolginov & Mitrofanov 1976; Draine & Weingartner 1996, 1997; Lazarian & Hoang 2007; Hoang & Lazarian 2008) becomes aligned with the grain’s short axis, and then with the magnetic field via precession (e.g., Martin 1971). The end result is that, if we look across magnetic field lines, the rotating grain will have its long axis orthogonal to the field lines, and accordingly dust emission will be linearly polarized with its electric vector normal to the sky-projected magnetic field.

A related phenomenon occurs at near-UV/optical/NIR wavelengths, where the light from background sources becomes linearly polarized as a result of dichroic extinction by the aligned dust grains (Davis & Greenstein 1951). Since extinction is higher for light vibrating parallel to the grain’s long axis, i.e., perpendicular to the field lines, the incoming light will be linearly polarized with its electric vector parallel to the sky-projected magnetic field. In fact, historically, the optical polarization caused by dust extinction led to the prediction that thermal dust emission would be polarized in the millimetre and sub-millimetre domains (Stein 1966).

Thus, polarized thermal dust emission carries important information on the interstellar magnetic field structure, on the

¹ *Planck* (<http://www.esa.int/Planck>) is a project of the European Space Agency (ESA) with instruments provided by two scientific consortia funded by ESA member states (in particular the lead countries France and Italy), with contributions from NASA (USA) and telescope reflectors provided by a collaboration between ESA and a scientific consortium led and funded by Denmark.

grain alignment mechanisms, and on the grain geometrical and physical properties. For example, polarization observations between 300 μm and 3 mm, essentially the domain of the *Planck* HFI instrument, can potentially discriminate between the polarizing grain materials, e.g., silicate and graphite dust versus silicate-only grains (Martin 2007; Draine & Fraisse 2009; Planck Collaboration Int. XXII 2014).

Since this far-IR emission is basically proportional to the dust mass along the LOS, sensitivity limits explain why detailed dust polarized emission was observed mostly in fairly dense, complex regions of the ISM (Dotson et al. 2000; Curran & Chrysostomou 2007; Matthews et al. 2009; Dotson et al. 2010), in general close to the Galactic plane. Measurements of the more diffuse medium were obtained at relatively low ($\geq 2^\circ$) angular resolution. At these large scales, the *Archeops* balloon experiment (Benoit et al. 2004; Ponthieu et al. 2005) detected the thermal dust emission polarization at 353 GHz. The highest frequency channel of *WMAP* (Page et al. 2007; Bennett et al. 2013), 94 GHz, picked up the long-wavelength Rayleigh-Jeans tail of the diffuse dust emission and its polarization (in addition to synchrotron emission).

The *Planck* satellite’s HFI instrument leads to the first all-sky survey of the polarized submillimetre and millimetre sky, where thermal dust emission dominates. At 353 GHz, the *Planck* data have an angular resolution of $5'$. The polarization sensitivity is expected to be such that, at a resolution of $15'$, ISM structures with $A_V = 1$ mag are detected with a relative uncertainty on the polarization fraction of about 40 % and an uncertainty on the polarization angle of about 30° (Pelkonen et al. 2009). These figures improve significantly at higher A_V and/or lower resolution. The polarized *Planck* data bring the first all-sky map of the polarization from a tracer of the interstellar matter. As such, they provide unprecedented information on the magnetic field geometry and the dust polarization properties relevant to the disk of the Milky Way (MW) and star forming regions, for which they provide statistical information that is missing in stellar polarization extinction data. It should be emphasized, however, that the dust polarized emission provides information mostly on the orientation of the sky-projected magnetic field and only very indirect indication about the angle of that field with respect to the plane of the sky, and it is expected to be almost insensitive to the field strength.

This paper presents the *Planck* polarization data and their large-scale statistical properties. A companion paper (Planck Collaboration Int. XX 2014) analyses the variations of the polarization fraction and angle described here, in comparison with the predictions from MHD simulations. Two other papers in this series provide a detailed analysis of the wavelength dependence of the dust polarization, as seen by the HFI instrument (Planck Collaboration Int. XXII 2014) and a comparison between the dust polarization at visible and submillimetre wavelengths (Planck Collaboration Int. XXI 2014).

In Sect. 2 we describe the data, including discussion of systematic effects and the effects of the CMB intensity and polarization. Maps are presented in Sect. 3, as well as the statistics of the data. Sect. 4 discusses the implications of the 353 GHz polarimetry for our understanding of the GMF structure, and the conclusions are drawn in Sect. 5. Two appendices discuss the smoothing of the noise covariance matrices, which is needed when the original data are averaged, as well as the de-biasing methods for obtaining polarization estimates.

2. Data

The *Planck* mission results are presented in Planck Collaboration I (2014) and the in-flight performance of the two focal plane instruments, the HFI (High Frequency Instrument) and the LFI (Low Frequency Instrument), are given in Planck HFI Core Team (2011) and Mennella et al. (2011), respectively. The data processing and calibration of the HFI data used here are described in Planck Collaboration VI (2014), Planck Collaboration VII (2014), Planck Collaboration VIII (2014), Planck Collaboration IX (2014) and Planck Collaboration X (2014). The data processing and calibration of the LFI data are described in Planck Collaboration II (2014), Planck Collaboration III (2014), Planck Collaboration IV (2014), and Planck Collaboration V (2014).

The *Planck* polarization and intensity data that we use in this analysis have been generated in exactly the same manner as the data publicly released in March 2013 and described in Planck Collaboration I (2014) and associated papers. Note however that the publicly available data includes only temperature maps based on the first two surveys. Planck Collaboration XVI (2014) shows the very good consistency of cosmological models derived from intensity only with polarization data at small scale (high CMB multipoles). However, as detailed in Planck Collaboration VI (2014) (see their Fig. 27), the 2013 polarization data are known to be affected by systematic effects at low multipoles which were not yet fully corrected, and thus, not used for cosmology. We have been careful to check that the Galactic science results in this paper are robust with respect to these systematics. The error-bars we quote include uncertainties associated with residual systematics as estimated by repeating the analysis on different subsets of the data. We have also checked our data analysis on the latest version of the maps available to the collaboration, to check that the results we find are consistent within the error-bars quoted in this paper.

The maps used include data from five independent consecutive sky surveys (called Survey1-Survey5) for HFI, taken six months apart. Due to the scanning strategy of the *Planck* mission, surveys taken one year apart (i.e. odd surveys 1 and 3 and even surveys 2 and 4) share the same observing pattern, which is different for even and odd surveys. Survey5 had a different scan pattern from the other odd-numbered surveys, owing to a change in the precession phase. The products also include data binned into the first and second halves of the *Planck* stable pointing periods, or “half-rings” (called HR1 and HR2). Both single-survey and half-ring data are used for consistency checks and to assess the level of systematic effects. Here, we only analyse the polarization data at 353 GHz, which is the highest frequency *Planck* channel with polarization capabilities and the one with the best S/N for dust polarization. We use the 30 GHz LFI data in our comparison of the dust emission at 353 GHz with the microwave and radio synchrotron emission presented in Sect. 4.4.

In the *Planck* map-making process (Planck Collaboration VIII 2014), measurements from various detectors at the same frequency are combined to obtain the Stokes parameters (I , Q , and U) at each position on the sky. The reconstructed polarization is a linear combination of the weighted differences between the signal from pairs of polarization sensitive bolometers (PSBs) with different orientations on the sky. The resulting maps of the *Planck* Stokes parameters Q and U used in this paper are shown in Fig. 1. The corresponding map of the observed polarization intensity $P = (Q^2 + U^2)^{1/2}$ is shown in Fig. 2. The intensity map used in this work is shown in Fig. 5.

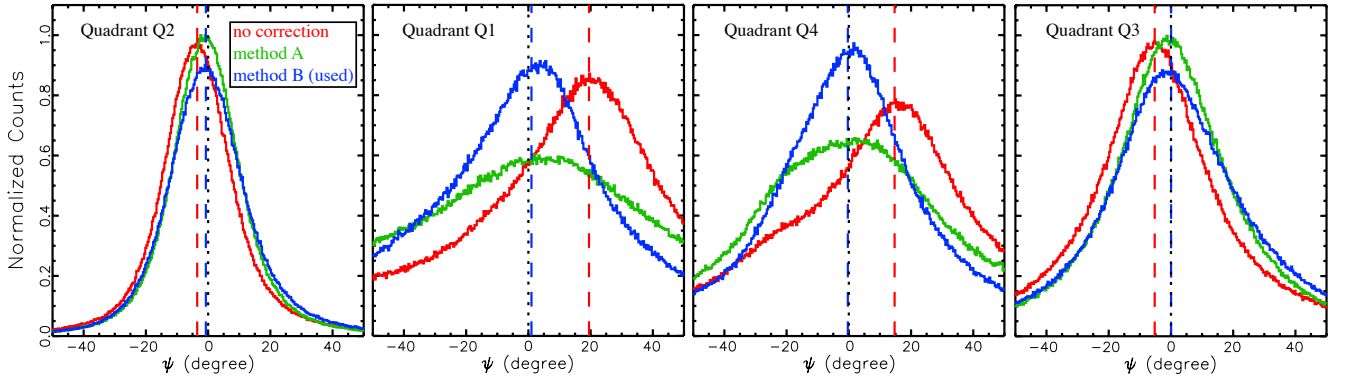


Fig. 3. Histograms of the observed polarized angle at the full data resolution towards the Galactic plane ($|b_{\text{II}}| < 5^\circ$) for the four Galactic quadrants. The various curves show data uncorrected for bandpass mismatch (red), and corrected using sky coupling coefficients derived either from ground (method A: green) or sky measurements (method B: dark blue). The vertical dashed lines show the peak value obtained from fitting the histograms with a Gaussian.

2.1. Conventions and notations

The relations between the observed Stokes parameters (I , Q , and U) and the polarization fraction (p) and polarization angle (ψ) are given by

$$p = \frac{\sqrt{Q^2 + U^2}}{I}, \quad (1)$$

and

$$\psi = 0.5 \times \arctan(U, Q), \quad (2)$$

where the two arguments function $\arctan(Y, X)$ is used to compute $\text{atan}(Y/X)$ avoiding the π ambiguity, such that

$$\begin{aligned} Q &= p \times I \times \cos(2\psi), \\ U &= p \times I \times \sin(2\psi). \end{aligned} \quad (3)$$

For the Stokes parameters provided in the *Planck* data, the angle convention above is with respect to Galactic coordinates with $-90^\circ < \psi < +90^\circ$ and $\psi = 0^\circ$ towards the Galactic north and positive towards the west (clockwise). Note that this convention is the one used in the HEALPix² software (Górski et al. 2005), but is different from the IAU convention (Hamaker & Bregman 1996), which is $\psi = 0^\circ$ towards north and positive towards the east (counterclockwise). The conversion between *Planck* Stokes parameters and the IAU convention is given by:

$$\psi_{\text{IAU}} = 0.5 \times \arctan(-U, Q). \quad (4)$$

In this paper, the tabulated angle values are given in the IAU convention.

2.2. Bandpass mismatch leakage correction

Owing to the way the polarization maps are constructed, any instrumental difference between detectors of the same channel may produce a fake polarization signal, even for unpolarized sky signal inputs. This is the case for the bandpass mismatch (BPM) between detectors that affects *Planck* polarization maps. In practice, the effect corresponds to a leakage term from intensity I into polarization Q and U . The BPM polarization leakage effect is therefore strongest in regions of high intensity, i.e., along the Galactic plane, and affects both p and ψ . Note that, since the 353 GHz intensity data used here are calibrated on the CMB

signal, no BPM leakage is produced by the CMB anisotropies. Other astrophysical emission sources, however, produce BPM polarization leakage.

Knowing the actual *Planck* sky scanning strategy and the orientations of the polarization sensitive bolometers in the focal plane, the BPM polarization leakage corrections can be estimated from the relative responses of each detector to a given sky astrophysical emission. The *Planck* collaboration is exploring different methods to compute the relative responses of detectors, as well as to produce total intensity maps for each sky emission source. Two methods have been used to determine the relative responses (Planck Collaboration IX 2014). The first one (method A) involves computing the BPM leakage between bolometers using the ground-measured bandpasses (Planck Collaboration IX 2014). The second one (method B) deduces the relative detector response on regions of the sky where we can obtain I , Q , and U maps for each detector individually. Note that this can only be performed in limited regions of the sky, outside the Galactic plane, which have been scanned in a large number of configurations, allowing for the full reconstruction of I , Q , and U per detector. A comparison between the two methods is presented in Planck Collaboration IX (2014).

When folding the above coefficients into the *Planck* scanning strategy, we have chosen to produce template maps $T_{b(\nu)}^X$ of the BPM leakage contribution for each frequency (ν) channel, for each bolometer ($b(\nu)$) and for each Stokes parameter (X being Q or U). The BPM polarization leakage correction is

$$L_\nu^X = \sum_{b(\nu)} R_{b(\nu)} I_\nu T_{b(\nu)}^X, \quad (5)$$

where $R_{b(\nu)}$ represents the detector relative responses and I_ν is the sky intensity. For the purpose of the study presented here, we only take into account BPM leakage from dust thermal emission, since this is the dominant term at 353 GHz. The template maps in Eq. 5 were computed using the *Planck* thermal dust model described in Planck Collaboration XI (2014). We used the standard *Planck* map-making procedure presented in Planck Collaboration VIII (2014). Note that the *Planck* 353 GHz channel also includes emission from the CO ($J = 3 \rightarrow 2$) line (see Planck Collaboration VI 2014), which should also in principle be included in the BPM leakage correction. This, however, is relatively weak with respect to dust thermal emission and the corresponding BPM effect is expected to be small compared to that

² <http://healpix.jpl.nasa.gov>

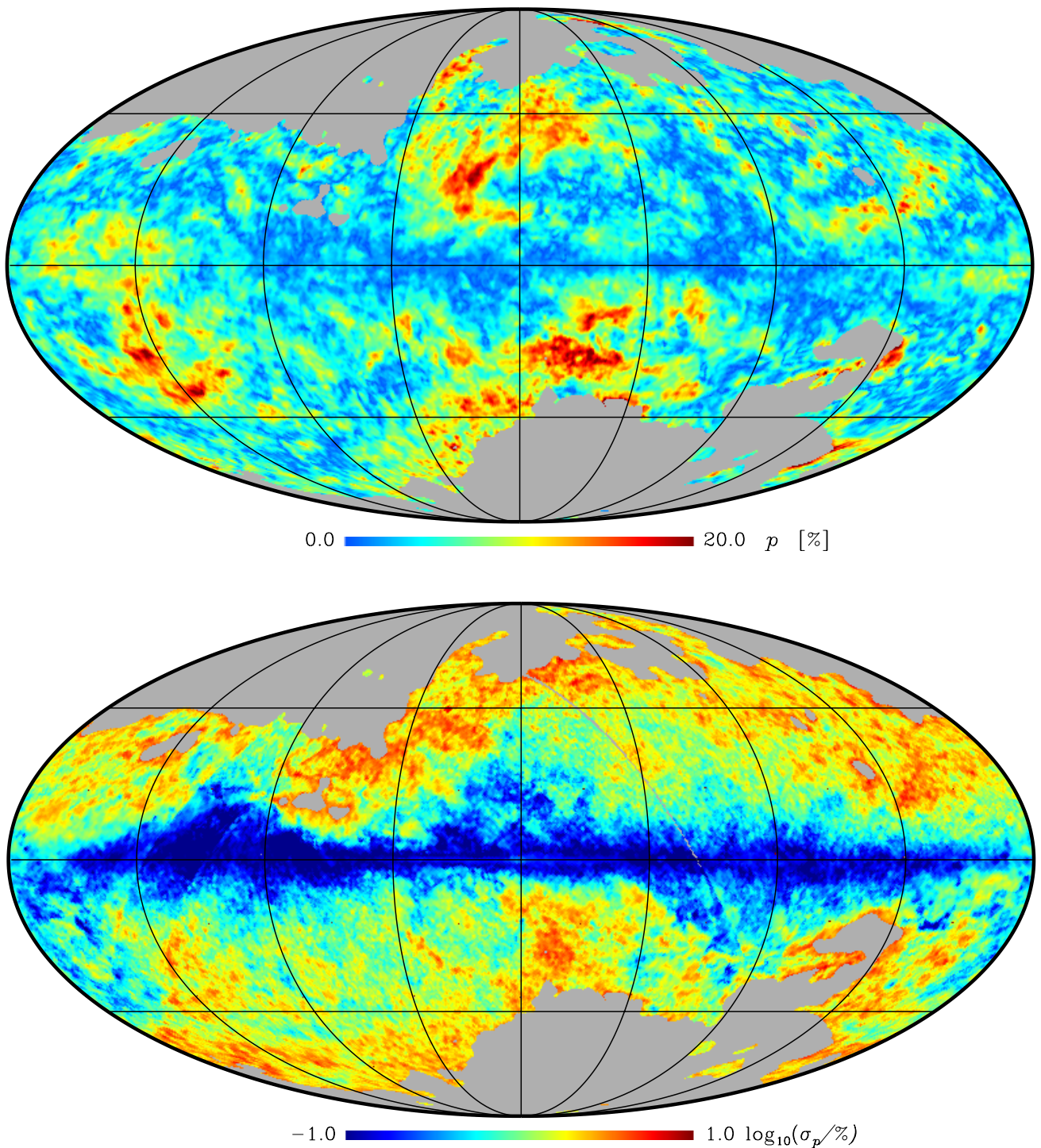


Fig. 4. *Upper:* Map of the 353 GHz polarization fraction p at 1° resolution. The colour scale is linear and ranges from 0% to 20%. *Lower:* Map of the 353 GHz polarization fraction uncertainty, σ_p , at 1° resolution in \log_{10} scale. The colour scale is from $\sigma_p = 0.1\%$ to $\sigma_p = 10\%$. The data are not shown in the grey areas where the dust emission is not dominant or where residuals were identified comparing individual surveys (see Sect. 2.4). The polarization fraction is obtained using the Bayesian method with a mean posterior estimator (see Sect. 2.3). The uncertainty map includes statistical and systematic contributions. The same mask as in Fig. 1 is applied.

from dust. Since we do not concentrate on regions with strong molecular emission in this paper, no correction was applied for the CO emission BPM leakage.

Figure 3 shows the effect of the correction for BPM on the observed distribution of polarization angles toward the plane of

the Milky Way ($|b_{\text{II}}| < 5^\circ$) in the four Galactic quadrants (Q1, Q2, Q3 and Q4, defined by $0^\circ < \ell_{\text{II}} < 90^\circ$, $90^\circ < \ell_{\text{II}} < 180^\circ$, $180^\circ < \ell_{\text{II}} < 270^\circ$, and $270^\circ < \ell_{\text{II}} < 360^\circ$, respectively). When no BPM leakage correction is applied, angles are observed to be distributed around $+20^\circ$ and -5° for the inner (Q1 and Q4)

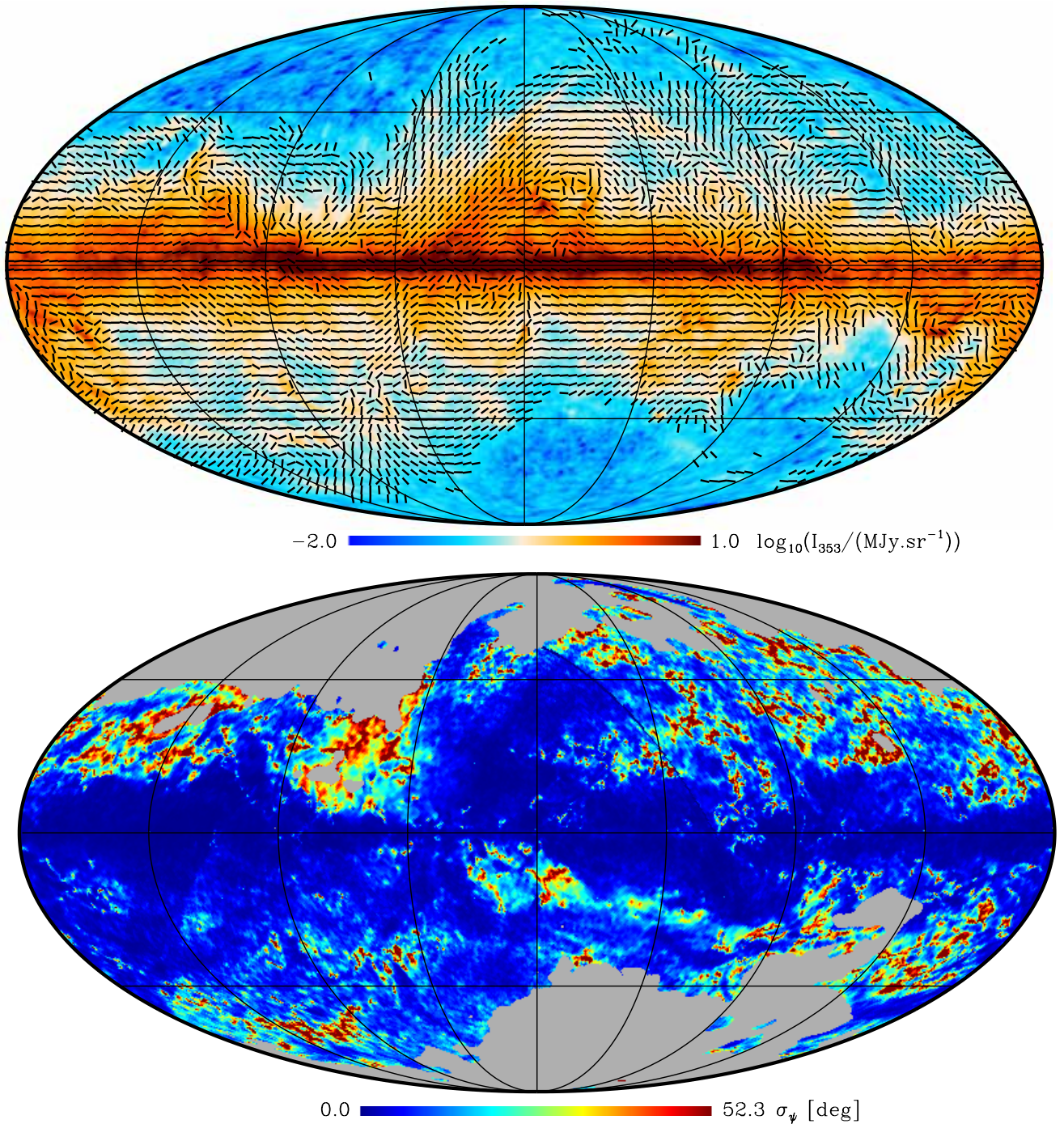


Fig. 5. *Upper:* Map of the apparent magnetic field ($\langle \mathbf{B}_\perp \rangle$) orientation. The normalized lines were obtained by rotating the measured 353 GHz polarization angles by 90° . The length of the polarization vectors is fixed and does not reflect polarization fraction. The colour map shows the 353 GHz emission in \log_{10} scale and ranges from 10^{-2} to 10 MJy sr^{-1} . *Lower:* Map of the 353 GHz polarization angle uncertainty (σ_ψ) at 1° resolution. The scale is linear from $\sigma_\psi = 0^\circ$ to $\sigma_\psi = 52.3^\circ$. The polarization angle is obtained using the Bayesian method with a mean posterior estimator (see Sect. 2.3). The uncertainty map includes statistical and systematic contributions. The same mask as in Fig. 1 is applied.

and outer (Q2 and Q3) MW regions, respectively. The difference in sign is due to the difference in average detector orientation during Galaxy crossings, resulting from the relative orientation of the scanning strategy and the Galactic plane. Using the two methods discussed above for the determination of the coupling coefficients leads to similar BPM leakage estimates. Note also that, since the magnetic field is expected to be statis-

tically aligned with the Galactic plane (see, e.g., Ferrière 2011), we expect the polarization direction towards the plane to be on average around $\psi = 0^\circ$. The fact that both correction methods bring the peak of the histograms toward this value confirms the validity of the BPM correction method used here. In the following, we adopted the coefficients from method B. We note, however, that although the situation is clearly improved by the BPM

leakage correction, the average observed angle distributions still peak a few degrees away from $\psi = 0^\circ$, with the same sign pattern as for the uncorrected data. This could in principle be due to incomplete correction. However, preliminary tests have shown that the remaining correction could be due to non-linearity in the analogue-to-digital conversion (ADC) of the signal, which produces an additional correction with the same sign as observed here and roughly the right amplitude.

We do not attempt here to fully assess the quality of the different corrections, but simply use them to estimate where on the sky the uncertainties in the corrections are small enough to be unimportant for this study. A plot of the BPM-leakage-corrected polarization angle versus the uncorrected polarization angle shows the magnitude of the correction, while the correlation coefficient gives a quantitative measure. For the different corrections considered above, the correlation coefficient is over 0.95 for most regions of the sky at $|b_{\text{II}}| > 5^\circ$. Above $|b_{\text{II}}| = 10^\circ$, the correlation coefficients are above 0.98, implying that the correction becomes very small. This is a natural result of the fact that the intensity that is leaking into polarization is brightest towards the Galactic plane. As measured from the difference between method A and B, the corresponding uncertainties on the polarization angle ψ and fraction p are $|\Delta\psi| < 10^\circ$ and $\Delta p < 1\%$, respectively, towards the inner Galactic plane. These uncertainties become less than the random errors away from the plane. However, BPM leakage corrections are probably not the dominant uncertainty at high galactic latitudes and very low signal levels, where other systematic effects remaining in the data become more important (see Sect. 2.4). For this reason, we do not discuss specifically the polarization properties in the lowest brightness sky area in this paper and defer this discussion to future papers.

The above discussion applies to the HFI data, but we will also compare the thermal dust emission at 353 GHz to the 30 GHz emission from LFI, which has a similar bandpass leakage issue. The LFI BPM correction is discussed in [Planck Collaboration II \(2014\)](#), where the principle difference is the presence of multiple astrophysical foregrounds, with different spatial and spectral distributions. The component separation products are therefore used in the LFI BPM correction. From a comparison of the different surveys, we estimate that the uncertainties are of the order $10\mu\text{K}$ in the polarized intensity and dominated by the noise rather than the leakage except in the innermost plane ($|\ell_{\text{II}}| < 30^\circ$ and $|b_{\text{II}}| < 3^\circ$), where the effect is only slightly above the noise level. For the polarization angle, we estimate the uncertainties as roughly 15° in the plane ($|b_{\text{II}}| < 5^\circ$) and 35° away. Again the uncertainty appears dominated by noise, with no obvious structure related to the bandpass leakage or scan pattern. We have also cross-checked with *WMAP* 23 GHz data and verified that the results in Sect. 4.4 are very similar.

2.3. Deriving polarization parameters

The polarization parameters I , p , and ψ are derived from the observed Stokes parameters I , Q , and U using the Bayesian method described in [Planck Collaboration Int. XXIII \(2014\)](#). This method extends that described in [Quinn \(2012\)](#) by using the full 3×3 noise covariance matrix of each pixel. The effective ellipticity, as defined in [Planck Collaboration Int. XXIII \(2014\)](#), characterizes the shape of the noise covariance matrix and couples all the terms in Q and U . $\epsilon_{\text{eff}} = 1$ corresponds to the case described in [Quinn \(2012\)](#), whereas $\epsilon_{\text{eff}} > 1$ means that the relation between C_{QQ} , C_{QU} , C_{UU} is not trivial, and there are asymmetries in the noise covariance matrix. We calculated ϵ_{eff}

for the *Planck* data used here. At 1° resolution it is normally distributed with a mean value of 1.12 and a standard deviation of 0.04. At the full *Planck* resolution, the distribution of ϵ_{eff} is a bit wider (standard deviation of 0.05), but the mean value does not change. Thus, although they are not very strong, the asymmetries of the noise covariance matrix cannot be neglected, and the Bayesian method is well suited for the analysis of the data. We use a flat prior on all 3 parameters p , ψ and I over a range centered on the conventional value of each parameter, and a width corresponding to 20σ , where σ is the conventional estimate for the uncertainty (see Appendix B.1). The range on p and ψ is further limited to $-1 < p < 1$ and $-90^\circ < \psi < 90^\circ$, respectively. We compute the 3D posterior probability distribution function (PDF) using 2^7 values on each axis over the parameter range. The values of the polarization parameters are obtained using the mean posterior (MP) estimator on the posterior 3D PDF. A comparison between the polarization parameters and uncertainties obtained with this method and using the conventional approach described in Appendix B.1 is shown in Fig. B.1 for the *Planck* data at 1° resolution.

When spatial smoothing is applied to the polarization data, Stokes parameter maps are convolved with a Gaussian kernel of the appropriate width using the dedicated smoothing software part of the HEALPix library, which guarantees proper transport of Q and U . The maps are then resampled to larger pixel size (as specified by the HEALPix N_{side} parameter) so as to preserve full sampling of the data (pixel size smaller than 1/2.4 times the data FWHM resolution). The corresponding smoothing of data covariances was performed using the method described in Appendix A. The corresponding smoothed maps of p and ψ are then computed as described above. The statistical uncertainties in p and ψ (σ_p^{stat} and $\sigma_\psi^{\text{stat}}$, respectively) have been estimated as described in Appendix B.3.

2.4. Impact of systematic effects, CIB, ZL and CMB

We assessed the level of contamination by systematic effects comparing the maps of p and ψ obtained at 1° resolution for the full *Planck* data with those obtained for the various individual *Planck* surveys (see Sect. 2). We constructed maps of systematic uncertainties on p and ψ (σ_p^{sys} and σ_ψ^{sys} , respectively) by averaging these differences over the *Planck* individual surveys. These were added to the statistical uncertainty maps σ_p^{stat} and $\sigma_\psi^{\text{stat}}$, to obtain the total uncertainty maps used in the rest of the analysis.

In this paper, we only show the *Planck* polarization data and derived quantities, where the systematic uncertainties are small, and where the dust signal dominates total emission. For this purpose, we defined a mask such that $\sigma_p^{\text{sys}} < 3\%$ and $I_{353} > 0.1 \text{ MJy sr}^{-1}$. We defined the mask at a resolution of 1° and smoothed it to 3° resolution to avoid complex edges. As a result, the maps shown exclude 21% of the sky. Note that a different mask is used for the polarization angle dispersion function, as defined in Sect. 3.3.

The cosmic infrared background (CIB) is due to emission from a large number of distant galaxies with random orientations and is expected to be, on average, unpolarized. However, it can contribute non-negligible emission at 353 GHz in low brightness regions of the sky and hence reduces the apparent degree of dust polarization. The zero level of the 353 GHz intensity map has been established by correlation with Galactic H I, using the method described in [Planck Collaboration XI \(2014\)](#), as was done for the publicly released 2013 maps. This offset is $0.0887 \text{ MJy sr}^{-1}$ (uncertainty $0.0068 \text{ MJy sr}^{-1}$) and was sub-

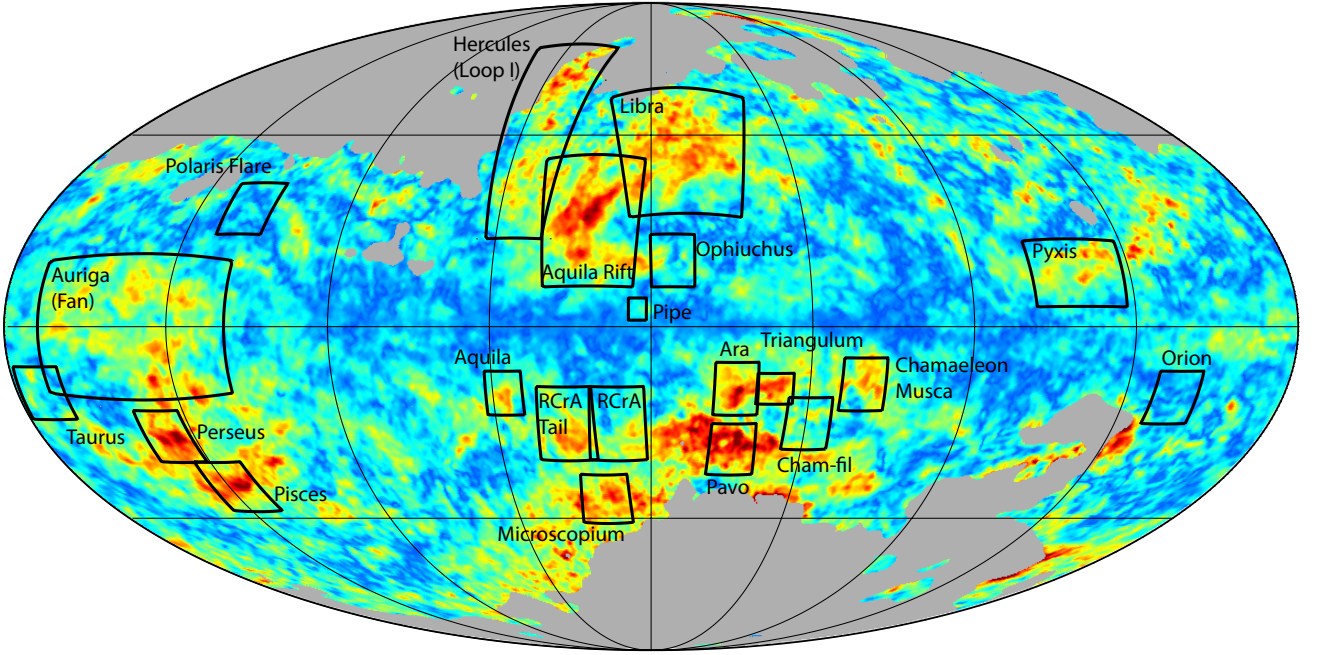


Fig. 6. Map of polarization fraction p from Fig. 4 with selected regions marked; statistics of these regions are given in Table 1.

Table 1. Polarization characteristics of individual regions shown in Fig. 6, computed at 1° resolution. The table gives the region name (column 1), the Galactic coordinates and extent of the region (columns 2–5), the minimum, mean, median, maximum, and standard deviation of p over the region (columns 6–10) and the median and standard deviation of ψ (columns 11–12). Note that the values of ψ are given in the IAU convention. Regions are ordered by increasing median p .

Region	ℓ_{II} [$^\circ$]	b_{II} [$^\circ$]	$\Delta\ell_{\text{II}}$ [$^\circ$]	Δb_{II} [$^\circ$]	min(p) [%]	mean(p) [%]	med(p) [%]	max(p) [%]	stdev(p) [%]	med(ψ) [$^\circ$]	stdev(ψ) [$^\circ$]
Polaris Flare.....	120.0	27.0	12.0	12.0	0.10	3.11	2.94	7.40	1.50	176.72	46.23
Orion.....	211.0	-16.0	12.0	12.0	0.08	3.22	2.97	10.23	1.73	177.17	42.87
Pipe.....	0.0	4.5	5.5	5.5	0.31	3.85	3.53	8.45	1.90	143.13	16.85
Ophiuchus.....	-6.0	15.0	12.0	12.0	0.11	5.11	4.59	12.22	2.60	0.84	20.69
Taurus.....	173.0	-15.0	12.0	12.0	0.16	5.08	4.83	11.62	2.19	129.00	60.11
RCrA.....	10.0	-22.0	15.0	17.0	0.30	6.80	6.71	13.97	2.94	11.62	15.42
Cham-fil.....	315.0	-22.0	12.0	12.0	1.40	6.95	6.78	15.29	2.22	14.32	8.56
Pyxis.....	-120.0	12.0	25.0	15.0	0.34	7.09	6.96	16.71	3.03	171.04	15.33
Aquila.....	42.0	-15.0	10.0	10.0	0.88	7.71	7.10	14.63	3.00	58.61	12.94
Auriga.....	145.0	0.0	50.0	30.0	0.12	7.55	7.58	18.64	2.76	1.69	12.20
RCrA-Tail.....	25.0	-22.0	15.0	17.0	1.66	8.63	8.40	15.53	3.16	170.71	14.65
Hercules.....	40.0	45.0	15.0	50.0	0.37	8.67	8.59	37.49	3.69	65.26	58.68
Libra.....	-10.0	40.0	30.0	30.0	0.34	9.35	9.90	21.39	3.42	20.03	23.72
Chamaeleon-Musca.....	300.0	-13.0	12.0	12.0	0.89	9.29	9.98	15.08	3.15	15.06	10.80
Aquila Rift.....	18.0	24.0	25.0	30.0	0.12	10.25	10.21	20.15	3.55	50.91	13.09
Ara.....	336.0	-14.0	12.0	12.0	3.15	11.18	10.85	21.09	2.99	177.49	8.90
Pisces.....	133.0	-37.0	12.0	12.0	4.32	12.10	11.72	20.81	3.22	15.60	4.99
Microscopium.....	15.0	-40.0	12.0	12.0	6.20	11.78	11.76	18.63	2.27	24.66	10.80
Triangulum.....	-35.0	-14.0	10.0	7.0	5.21	12.12	12.12	17.14	2.82	6.66	4.95
Perseus.....	143.0	-25.0	12.0	12.0	5.66	12.68	12.68	21.10	3.20	9.68	5.96
Pavo.....	336.0	-28.0	12.0	12.0	3.60	14.13	14.33	21.77	3.61	14.29	7.99

tracted from the intensity map we use, which therefore does not contain the CIB monopole. We added the corresponding uncertainty to the intensity variance, so that the statistical uncertainties on p include the uncertainty on the CIB subtraction.

The zodiacal light (ZL) has a smooth distribution on the sky. From the model constrained by its detection in the *Planck* bands (Planck Collaboration XIV 2014), its median intensity at 353 GHz is 1.9×10^{-2} MJy sr $^{-1}$ over the sky area studied here,

and reaches $\approx 4.3 \times 10^{-2}$ MJy sr $^{-1}$) in dust lanes near the ecliptic plane. Its polarization in the submillimetre is currently unconstrained observationally. Since this intensity is subdominant over most of the sky fraction and the polarization level of ZL is currently unknown, we apply no correction for the possible contribution of ZL. We note that, if ZL was assumed unpolarized, subtracting its intensity would raise the observed polarization levels by about 0.5% of the observed polarization fraction, on

average over the sky region studied here, and would not change the observed polarization angles. We have checked that no noticeable systematic variation of the polarization fraction is detected in our maps along zodiacal dust lanes.

CMB fluctuations are polarized at a level of 0.56 mK (Kovac et al. 2002) at a resolution of about 1° , which corresponds to 1.6×10^{-4} MJy sr $^{-1}$ at 353 GHz. In the mask we use here, the effect of CMB polarized fluctuations is therefore negligible and we did not attempt to correct for those fluctuations.

No additional correction was applied to the data.

2.5. External data

In Sect. 4.4, we compare the *Planck* HFI polarization maps with low-frequency radio and microwave observations that are dominated by synchrotron emission over most of the sky. These include:

- the 408 MHz total intensity map of Haslam et al. (1982) from the LAMBDA³ site;
- the 1.4 GHz total intensity map of the northern (Reich 1982; Reich & Reich 1986) and southern (Reich et al. 2001) sky;
- the 1.4 GHz polarized intensity maps of the northern (Reich 1982) and southern (Reich & Reich 1986) sky;

For the analysis in Sect. 4.4, the *Planck* HFI and LFI maps are smoothed to 1° FWHM resolution to match these radio data and downgraded to $N_{\text{side}} = 256$. Most of the 1.4 GHz maps are available on the Bonn survey site⁴ as FITS images in Cartesian coordinates. They are converted into HEALPix using the procedure described in Paradis et al. (2012) and are made available in this form on the CADE site⁵. The resolution of the observations is roughly 1° , so no additional smoothing is applied to the radio data. The total intensity map at 1.4 GHz is estimated to have an offset of 2.8 K (Reich et al. 2004) due to the combination of zero-level calibration uncertainty, unresolved extragalactic sources, and the CMB, so this was subtracted from the data.

The total intensity data include thermal bremsstrahlung (free-free) emission, particularly in the plane. This is not negligible at 408 MHz or 1.4 GHz. We use the *WMAP* MEM free-free solution (Gold et al. 2011) to subtract it. We note that this free-free template likely includes anomalous dust emission, and there are indications that it is an overestimate by roughly 20 to 30% (Alves et al. 2010; Jaffe et al. 2011). Since synchrotron dominates over free-free emission at low radio frequencies, even on the Galactic plane, the uncertainties on the free-free correction are not expected to affect the qualitative comparison with dust emission in this paper. But the MEM template is not sufficiently accurate to correct for free-free when the synchrotron is subdominant at 30 GHz. Furthermore, the 30 GHz total intensity also includes anomalous dust emission for which we have no correction. We therefore do not use 30 GHz in total intensity, but only in polarization.

3. Description of the *Planck* polarization maps

Figure 4 shows the maps of the polarization fraction (p) at a resolution of 1° . Figure 5 shows the map of the polarization direc-

³ <http://lambda.gsfc.nasa.gov>

⁴ <http://www.mpi-fr-bonn.mpg.de/survey.html>. The southern part of the 1.4 GHz total intensity data was provided by W. Reich (private communication).

⁵ Analysis Center for Extended Data, <http://cade.irap.omp>

tion, also at a resolution of 1° . Both figures also show the corresponding map of the total uncertainty, which includes the contribution from statistical and systematic uncertainty estimates, as described in Sect. 2.4. The maps were masked as described in Sect. 2.4 in regions where large residual systematic uncertainties were evident or where the total intensity at 353 GHz is not dominated by dust emission. Figures 4 and 5 were constructed using the mean posterior method described in Appendix B.3 and are discussed in Sects. 3.1 and 3.2. In Fig. 6 we highlight several regions of interest that we will discuss below; parameters of these regions are given in Table 1.

3.1. Polarization fraction

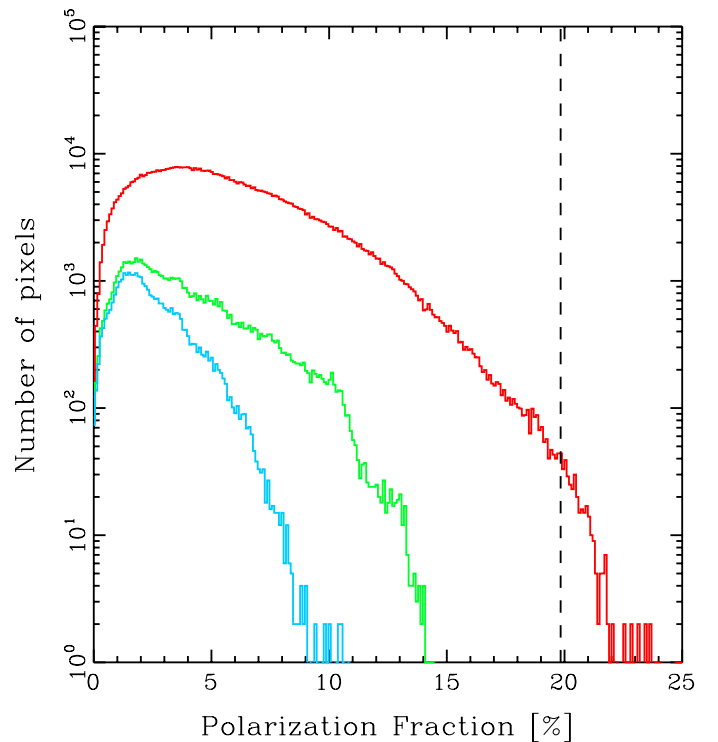


Fig. 7. Histograms of the observed polarization fraction at 1° resolution for the whole sky shown in Fig. 1 (red), the Galactic plane within $|b_{\text{II}}| < 5^\circ$ (green) and the inner Galactic plane within $|b_{\text{II}}| < 5^\circ$ and $|l_{\text{II}}| < 90^\circ$ (blue). The vertical dashed line shows the maximum value p_{max} discussed in Sect. 4.1.

As seen from Fig. 4, the measured polarization fraction shows significant variations on the sky. One of the aims of this paper is to characterize those variations and to try to understand their origin. These characteristics are compared to those of polarized emission maps computed in simulations of anisotropic MHD turbulence in a companion paper (Planck Collaboration Int. XX 2014).

Figure 4 shows that the polarization fraction of the thermal dust emission can reach up to about 20% in several large-scale regions of the sky. This is particularly the case in the second Galactic quadrant (a region known as “the Fan”) ($l_{\text{II}} \approx 140^\circ$, $b_{\text{II}} \approx 0^\circ$), the Perseus area ($l_{\text{II}} \approx 144^\circ$, $b_{\text{II}} \approx -30^\circ$), the Loop I area ($l_{\text{II}} \approx 16^\circ$, $b_{\text{II}} \approx +24^\circ$) and a region we call Microscopium ($l_{\text{II}} \approx 336^\circ$, $b_{\text{II}} \approx -20^\circ$). The large-scale distribution of these regions is consistent with predictions from the Galactic mag-

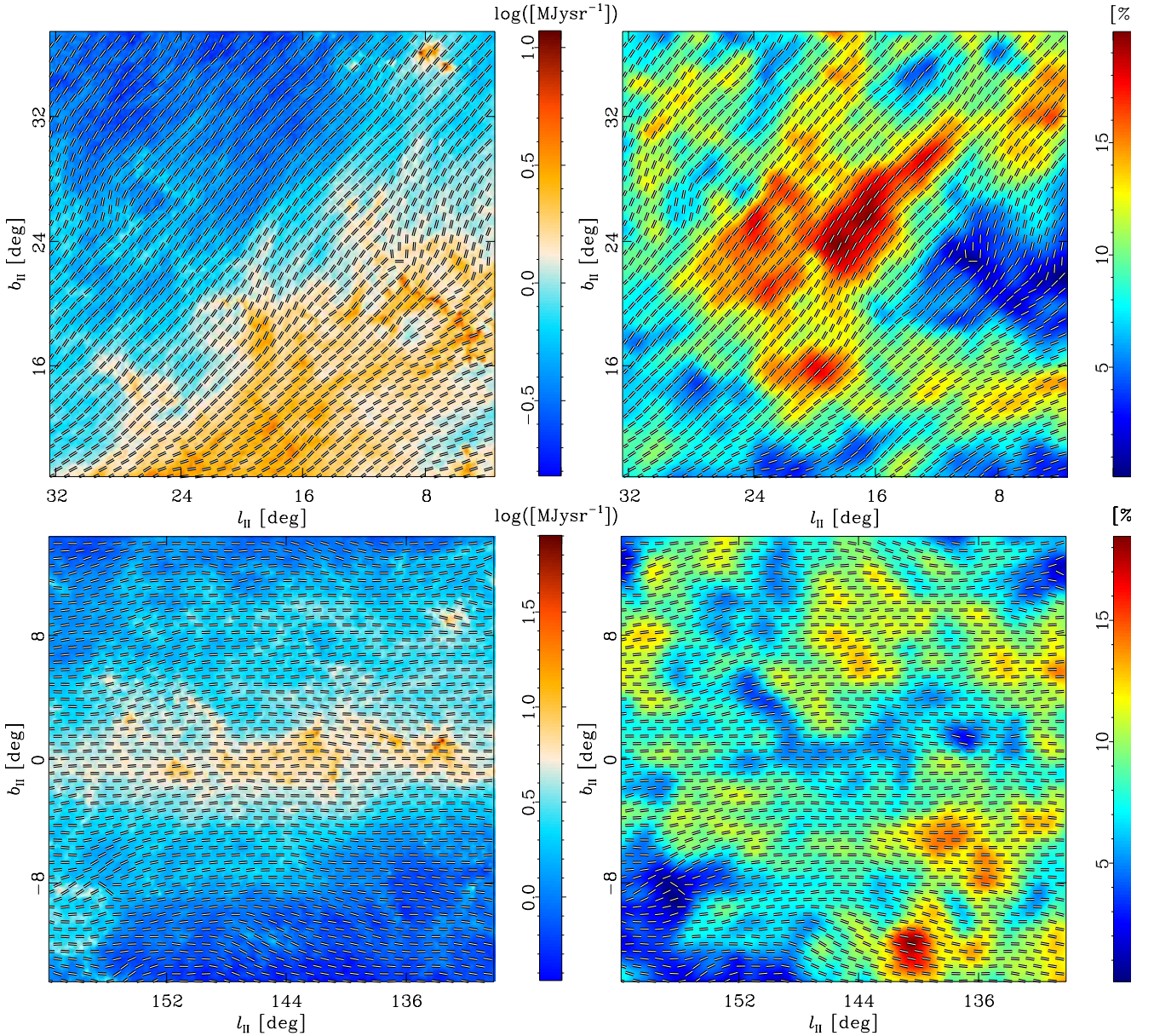


Fig. 8. Maps of the intensity (*left column*) and polarization fraction (*right column*) at 353 GHz for two of the most polarized regions: Aquila Rift (*upper*), and the Fan (*lower*). The intensity map is shown at the full *Planck* resolution, while the polarization information is shown at a resolution of 1° . The normalized lines show the orientation of the apparent magnetic field. The length of the polarization vectors is normalized and does not reflect polarization fraction.

netic field model used in the Planck Sky Model (Delabrouille et al. 2013). This model, based on a simple description of the spiral magnetic field structure of the Milky Way, was optimized to match the *WMAP* and *Archeops* data (e.g., Fauvet et al. 2011, 2012). It predicts a depolarization factor that has a minimum in the Galactic plane towards the anticentre at a position corresponding roughly to that of the Fan region and shows two strong minima at mid-latitude toward the inner Galaxy $\ell_{\text{II}} \simeq 0^\circ$ and $|b_{\text{II}}| \simeq 45^\circ$ which match fairly well with the highly polarized regions detected with *Planck* around the Aquila Rift and Pavo, above and below the galactic plane, respectively.

Figure 7 shows the histogram of the polarized fraction p over the sky fraction shown in Fig. 4, the whole Galactic plane ($|b_{\text{II}}| < 5^\circ$) and the inner Galactic plane ($|b_{\text{II}}| < 5^\circ$, $|\ell_{\text{II}}| < 90^\circ$) at a resolution of 1° . In the plane, the most likely value of p is a few

percent while the rest of the mid-latitude sky has a wider distribution, with a peak of the histogram near 4%. The maximum p values can reach about 20%. A more accurate determination of the maximum p value p_{max} , taking into account the effects of data resolution and noise, is given in Sect. 4.1 and leads to a similarly high value. We note that this maximum value is much higher than values reported previously from ground-based observations in the submillimetre. This is mainly because such low brightness regions are too faint to be observed from the ground, and because higher column density and brighter regions, which can be observed from the ground, have a tendency to be less polarized than faint regions (see Sect. 4.2). We also note that the high polarization fractions observed here are more consistent with the value inferred from the *Archeops* measurements at 353 GHz, which was derived to be as high as 10–20% (Benoit

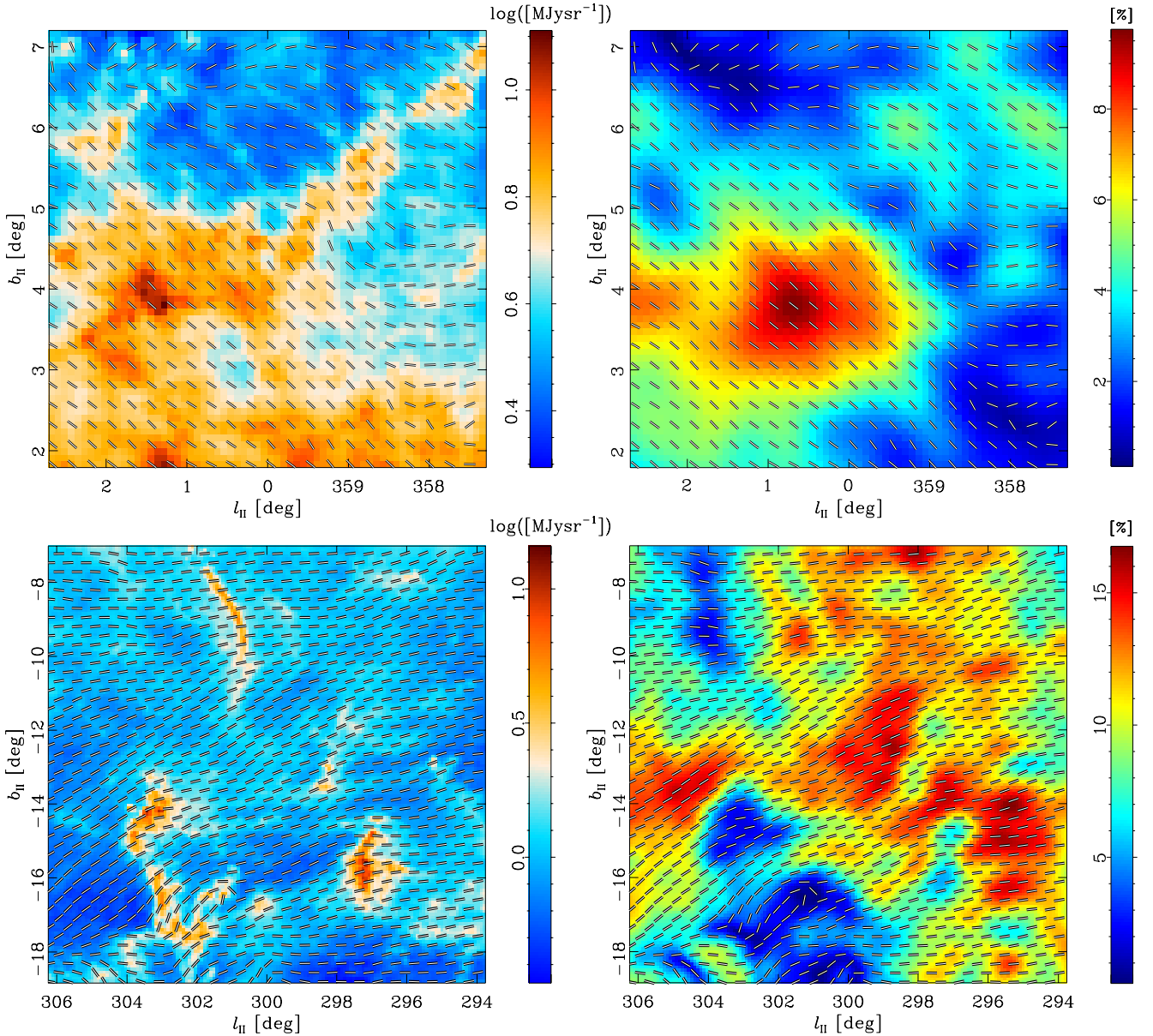


Fig. 9. Same as Fig. 8 for the Pipe Nebula (*upper*) and Musca (*lower*) regions. The polarization data is shown here at a resolution of $30'$.

et al. 2004) along the outer Galactic plane, a region which includes the Fan region.

Figures 8, 9, and 10 show maps around some of the regions outlined in Fig. 6 and listed in Table 1. Figure 8 shows the Aquila Rift and Fan regions, which show high polarization fraction. These highly polarized regions are generally located in rather low intensity parts of the sky (e.g., Microscopium, Libra, Pavo or Ara), or on the edge of bright regions (e.g., the Aquila Rift). They are also located in regions of the sky where the polarization direction is rather constant over very large areas. For instance, in the Fan region, the magnetic field is oriented almost completely parallel to the Galactic plane (i.e., polarization is orthogonal to the plane) with high accuracy over a region spanning more than 30° , where the polarization fraction consistently has $p > 8\%$ and reaches $p \simeq 15\%$ in some areas. Similarly, the highly polarized Aquila Rift region has a \mathbf{B} -field sky projection aligned with the elongated structure of the ridge and the nearby Loop I

over most of the extent of the source, and the polarization fraction there reaches up to 20%. The highly polarized region is in fact located on the gradient of the dust emission of the Aquila Rift, and mid-way between the Aquila Rift itself and the radio emission of Loop I. In the Perseus region, the large polarization also appears in fairly low brightness regions, where the orientation of the field is coherent over regions of the sky with typical sizes of a few degrees. Some of these structures have been detected in polarized light at other wavelengths. For instance, the Fan, Perseus, and Loop I regions seem to have counterparts detected in polarized thermal dust and synchrotron emission, as well as in Faraday RM surveys of polarized emission at radio frequencies, such as the Global Magneto-Ionic Medium Survey (GMIMS; Wolleben et al. 2010b) and the WMAP foreground emission (Gold et al. 2011; Berkhuijsen 1971; Ruiz-Granados et al. 2010; Jansson & Farrar 2012a, and references therein). In particular, from the RM data of GMIMS a significant portion

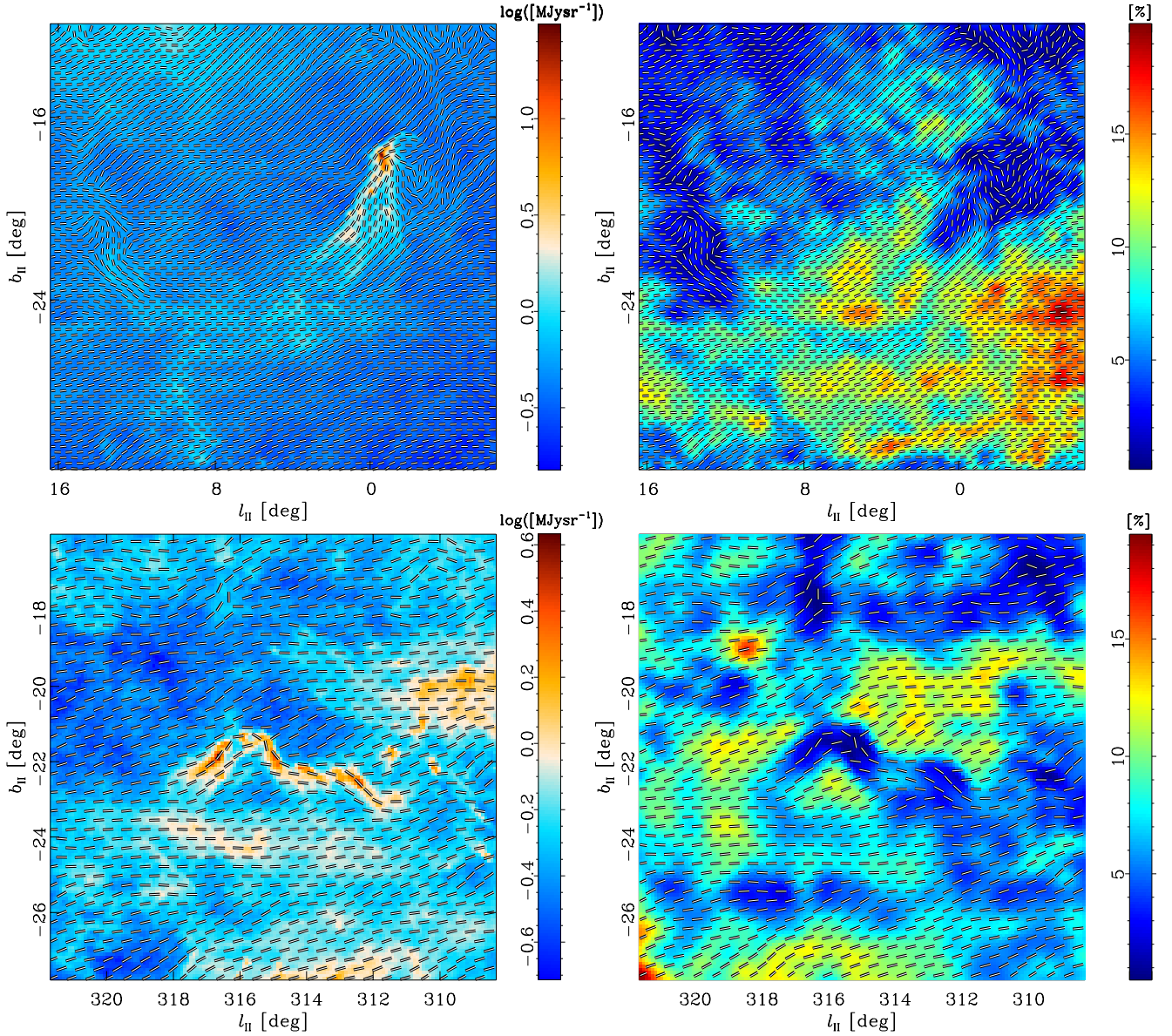


Fig. 10. Same as Fig. 9 for regions RCrA and RCrA-Tail (*upper*) and Cham-fil (*lower*). The polarization data is shown here at a resolution of $30'$.

(about 5 %) of the sky has been identified to be dominated by the magnetic field around a local H I bubble (at a distance of 100 pc) whose edges seem to coincide with the Loop I region described above (Wolleben et al. 2010a). In general, such regions are identified with nearby Galactic structures (e.g., supernova remnants and bubbles), which can even distort the underlying more regular large-scale pattern of the Galactic magnetic field. Finally, other regions, such as Microscopium, have almost no known counterpart structure in other wavelengths. The area around Ara and Triangulum has been identified only as a region with warmer dust in Planck Collaboration XIX (2011). Here too, the polarization fraction is typically $p > 10\%$ (see also Sect. 4).

As seen in Figs. 4 and 7, the inner Galactic plane shows much lower polarization fractions than the highly polarized regions described above. This is partly due to the larger depolarization factor caused by the overall structure of the MW magnetic field. It is also likely due to the fact that the ISM in the MW contains

a collection of dense clouds, which have a general tendency to exhibit lower polarization fractions (see Sect. 4.2).

Note that the polarization map exhibits narrow features where polarization drops (see for instance the one crossing the Polaris Flare region in Fig. 6). These are sometimes regions with higher gas column density N_{H} , but not always. They can also be regions where the orientation of the field changes more abruptly (see Sect. 3.2 for a full discussion).

3.2. Polarization angle

Figure 5 shows the large-scale distribution of the polarization direction. In the figure, the direction shown by the normalized lines is that of the observed polarization direction (ψ) rotated by 90° . The figure therefore shows the orientation of the apparent magnetic field ($\langle \mathbf{B}_\perp \rangle$). In the simplified case that the direction of \mathbf{B} remains homogenous along the LOS, $\langle \mathbf{B}_\perp \rangle$ measures the projection of \mathbf{B} onto the plane of the sky, i.e., perpendicular to

the LOS. However, in the more realistic case of a disordered \mathbf{B} structure and inhomogeneous dust distribution along the LOS, it is important to remember that $\langle \mathbf{B}_\perp \rangle$ is a LOS-averaged quantity, weighted by dust emission.

Figure 5 shows that, towards the Galactic plane, $\langle \mathbf{B}_\perp \rangle$ is mostly oriented along the plane, corresponding to a polarization angle close to 0° . This is especially the case towards the outer MW regions. There are a few exceptions, in particular toward the tangent points (Cygnus X, $\ell_{\text{II}} \simeq 81^\circ$, $b_{\text{II}} \simeq 0^\circ$; Carina, $\ell_{\text{II}} \simeq 277^\circ$, $b_{\text{II}} \simeq -9^\circ$), where the polarization signal is actually the smallest in the plane due to the magnetic field pointing along the LOS in those regions. This was already noticed in Benoit et al. (2004). We also note that the homogeneity of the field orientation being parallel to the plane extends away from the plane and up to $|b_{\text{II}}| \simeq 10^\circ$ in many regions (in particular the Fan). At intermediate latitudes, the field orientation follows a few of the well known filamentary intensity structures of the local ISM. In particular, this is the case for the Aquila Rift and Loop I, where the structure of $\langle \mathbf{B}_\perp \rangle$ follows the intensity flare and loop elongation. As addressed earlier, this orientation of $\langle \mathbf{B}_\perp \rangle$ in those regions was already noted in the synchrotron polarized maps of *WMAP* (Gold et al. 2011). Other regions, however, show a variety of relative orientations between the field projection and intensity structures, which can also be orthogonal in some instances.

3.3. Polarization angle dispersion function

In order to quantify the regularity of the \mathbf{B} field revealed by the polarization measurements, we use the polarization angle dispersion function (see Serkowski 1958; Kobulnicky et al. 1994; Hildebrand et al. 2009) given by

$$\Delta\psi^2(\mathbf{x}, \delta) = \frac{1}{N} \sum_{i=1}^N \Delta\psi_{xi}^2, \quad (6)$$

where $\Delta\psi_{xi} = \psi(\mathbf{x}) - \psi(\mathbf{x} + \delta_i)$ is the angle difference between $\psi(\mathbf{x})$, the polarization angle at a given sky position \mathbf{x} (the central pixel), and $\psi(\mathbf{x} + \delta_i)$ the polarization angle at a sky position displaced from the centre by the displacement vector δ_i . The average in Eq. 6 is taken over an annulus of radius $\delta = |\delta|$ (the ‘‘lag’’) and width $\Delta\delta$ around the central pixel and containing N pixels. In practice, $\Delta\psi_{xi}$ is computed from the Stokes parameters as

$$\Delta\psi_{xi} = \frac{1}{2} \arctan(Q_i U_x - Q_x U_i, Q_i Q_x + U_i U_x), \quad (7)$$

where indices x and i stand for the central and displaced values, respectively.

The polarization angle dispersion function measures the inhomogeneity of the polarization direction orientation, irrespective of absolute direction. It provides important information on the magnetic field distribution and orientation (see, e.g., Falceta-Gonçalves et al. 2008; Poidevin et al. 2013). Regions where the sky projection of the magnetic field is well ordered will have $\Delta\psi \simeq 0^\circ$, while regions with a twisted or disordered \mathbf{B} field can in principle have up to $\Delta\psi = 90^\circ$. In addition, since the *Planck* convention for Q and U is defined with respect to the Galactic coordinate system, even a homogeneous field would produce $\Delta\psi \neq 0^\circ$, due to the coordinate singularity at the poles. In order to avoid this, we have rotated Q and U locally to a different coordinate system so that the current point is at the equator of the new system, before applying Eq. 7. When the signal is dominated by noise, $\Delta\psi$ converges to $\Delta\psi = \pi/\sqrt{12} (\approx 52^\circ)$, which can be identified as a bump in the histograms of $\Delta\psi$. The angle

dispersion function $\Delta\psi$ is generally observed to increase with δ , as the coherence is gradually lost when going further away from a given point of the sky. It is expected to increase linearly with lag in the presence of an ordered magnetic field and to steepen at small lags due to either the turbulent component of the magnetic field or the angular resolution of the data used (see, e.g., Hildebrand et al. 2009). The dependence of $\Delta\psi$ on lag δ can be better probed from the analysis of individual regions at higher resolution, either in emission or in absorption towards stellar clusters (Magalhães et al. 2005; Falceta-Gonçalves et al. 2008; Franco et al. 2010).

Like other quadratic functions, $\Delta\psi$ is biased positively when noise is present. As described in Hildebrand et al. (2009), $\Delta\psi$ can be debiased using

$$\Delta\psi_{\text{db}}^2(\delta) = \Delta\psi^2(\delta) - \sigma_{\Delta\psi}^2, \quad (8)$$

where $\sigma_{\Delta\psi}^2$ is the variance on $\Delta\psi$. In the conventional approach, $\sigma_{\Delta\psi}^2$ can be expressed as a function of σ_ψ through partial derivatives as

$$\sigma_{\Delta\psi}^2 = \frac{1}{N^2 \Delta\psi^2} \left(\left(\sum_{i=1}^N \Delta\psi_{xi} \right)^2 \sigma_\psi^2 + \sum_{i=1}^N \Delta\psi_{xi}^2 \sigma_\psi(\delta_i)^2 \right). \quad (9)$$

However, this approximation is valid only close to the solution and leads to a poor estimate of the bias at low S/N. Nonetheless, it is clear from Eqs. 9 and B.7 that regions with low polarization having higher values of σ_p/p will have higher σ_ψ and therefore more biased $\Delta\psi$.

In order to assess the importance of the bias, we use the two independent half-ring maps of the *Planck* data to compute an unbiased estimate of $\Delta\psi$ as

$$\Delta\psi_H^2(\delta) = \frac{1}{N} \sum_{i=1}^N \prod_{h=1}^2 \Delta\psi_{xi}^H, \quad (10)$$

where $\Delta\psi_{xi}^H$ is the angle difference for a half-ring map H , i.e., $\Delta\psi_{xi}^H = \psi^H(\mathbf{x}) - \psi^H(\mathbf{x} + \delta_i)$. In practice, $\Delta\psi_{xi}^H$ is computed as

$$\Delta\psi_{xi}^H = \frac{1}{2} \arctan(Q_i^H U_x^H - Q_x^H U_i^H, Q_i^H Q_x^H + U_i^H U_x^H). \quad (11)$$

Although $\Delta\psi_H$ is unbiased, it suffers from higher noise, since only half of the *Planck* data are used. Note also that, unlike $\Delta\psi^2$, $\Delta\psi_H^2$ can be negative.

We evaluate $\Delta\psi$ from the full *Planck* survey (we call this estimate simply $\Delta\psi$ by default) and $\Delta\psi_H$ at each pixel of the map using Eqs. 7 and 11, respectively. We also perform a Monte Carlo noise simulation on I , Q , and U for each pixel using the full covariance matrix using Eq. A.23, and assuming that different pixels have independent noise and that the half-ring maps have independent noise. This simulation is used to construct the PDF of $\Delta\psi^2$ and $\Delta\psi_H^2$ using 1000 noise samples. We then compute the mean posterior estimates ($\overline{\Delta\psi^2}$ and $\overline{\Delta\psi_H^2}$) and variances ($\sigma_{\Delta\psi^2}^2$ and $\sigma_{\Delta\psi_H^2}^2$) of $\Delta\psi^2$ and $\Delta\psi_H^2$ by integrating over the PDF.

Figure 11 shows the sky distribution of $\Delta\psi$ computed from the full survey at 353 GHz at 1° resolution for a lag of $\delta = 30'$ and $\Delta\delta = 15'$. Figure 12 shows the same maps obtained from the half-ring survey correlation ($\Delta\psi_H$), as well as for individual *Planck* surveys. The mask used in these figures was obtained from the uncertainty on $\Delta\psi$, $\sigma_{\Delta\psi}$, derived from the Monte Carlo analysis described above. The mask is such that the S/N on $\Delta\psi$ is larger than 3 ($\Delta\psi/\sigma_{\Delta\psi} > 3$) and retains 52% of the sky at the

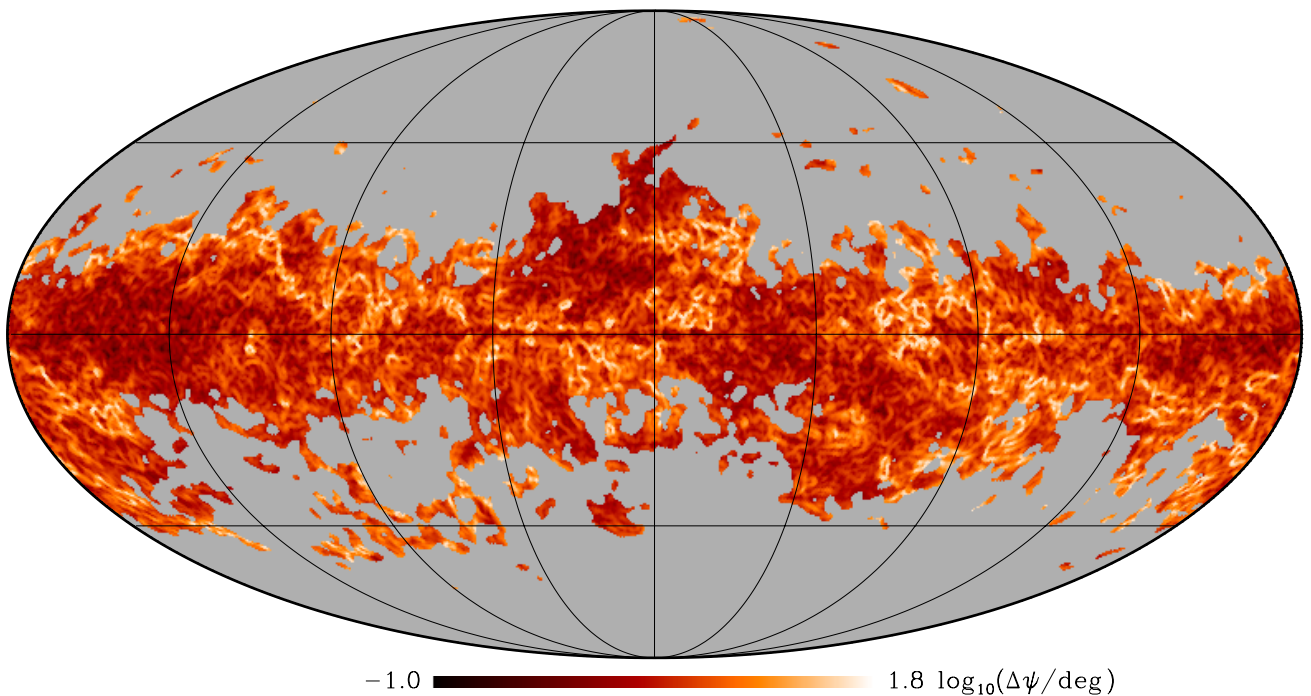


Fig. 11. Map of the polarization angle dispersion function $\Delta\psi$ at 353 GHz with 1° resolution and for lag $\delta = 30'$. The map is shown in \log_{10} scale over the range $0.1^\circ < \Delta\psi < 70^\circ$. Only sky regions where the S/N on $\Delta\psi$ is larger than 3 are shown (see text).

adopted analysis resolution of 1° . The differences between individual panels of Fig. 12 are smaller than the 33% statistical uncertainty in the determination of $\Delta\psi$ within the mask. Figure 13 shows the histogram of $\Delta\psi$ within the above mask, as well as in subsets of the data with various cuts in p . It shows that most sky pixels with reliable $\Delta\psi$ have low $\Delta\psi$ values, and that most of these pixels have large polarization fractions, above $p = 5\%$.

As can be seen in Figs. 11 and 12, a similar structure for $\Delta\psi$ appears in all estimates in the selection mask, clearly showing that these structures are not caused by a single subsection of the data. We note that, outside the mask, $\Delta\psi$ shows structures similar to those observed in the mask. However, significant differences appear in some regions, in particular between odd and even *Planck* surveys. We attribute those to an imperfect band-pass mismatch correction or to the fact that no ADC correction has been applied here. We have also conducted tests in order to quantify the possible noise-induced bias on $\Delta\psi$. Those are described in Appendix C. Figure 14 shows the map of $\Delta\psi$ when the resulting estimate of the bias has been subtracted. Comparison with Fig. 11 shows that the effect of bias essentially reduces low $\Delta\psi$ values, but does not explain the patterns observed in the map. We therefore conclude that the structures seen in the map of the polarization angle dispersion function $\Delta\psi$ are real, rather than being induced by noise and/or bias. In the rest of the analysis carried out here, we use the map of $\Delta\psi$ derived from the full survey and only consider pixels where the S/N on $\Delta\psi$ as derived from our Monte Carlo analysis is larger than 3. The resulting map is shown in Fig. 11. Further analysis of the angular distribution function and the comparison with the polarization fraction are presented in Sect. 4.3.

Figure 15 shows the values of the observed $\Delta\psi$ averaged in bins of p as a function of the lag value. As expected, the angle dispersion function increases steadily with increasing lag. Lower values of $\Delta\psi$ systematically correspond to higher p values, as

discussed in Sect. 4.3. Figure 16 shows details of $\Delta\psi$ for a few selected regions.

4. Discussion

In this section, we analyse the observed variations of the polarization fraction and angle at 353 GHz and discuss the possible implications in terms of dust physics and magnetic field structure.

4.1. Maximum polarization fraction

The maximum dust polarization fraction (p_{\max}) is a parameter of importance for the physics of dust and its alignment with respect to the magnetic field, because it directly provides an upper limit to the intrinsic polarization fraction, p_0 , for the optimal orientation of the magnetic field, i.e., in the plane of the sky. It is also important for the CMB component separation in polarization, as it sets the maximum amplitude of dust polarization. The observed p values are, however, affected by averaging in the beam and along any given LOS. Variations of the \mathbf{B} direction within the beam or along the LOS necessarily result in a decrease of the observed p . Similarly, dilution by an additional unpolarized source of emission, such as free-free or spinning dust emission, can only decrease p . Therefore, derived values of p_{\max} can only be lower limits to the intrinsic polarization fraction p_0 .

Here, we use the *Planck* maps at 353 GHz to evaluate p_{\max} . Since p is a biased quantity and since noise depends upon the data resolution, the observed maximum polarization fraction depends upon resolution. It is therefore crucial to take uncertainties into account. Figure 17 shows the sky fraction, $f_{\text{sky}}(p > p_v)$, where the observed polarization fraction is higher than a given value p_v as a function of that p_v . The various curves are for data resolutions of 1° , $30'$, and $15'$. The coloured area shown correspond to $f_{\text{sky}}(p \pm 4\sigma_p > p_v)$ for the various resolutions.

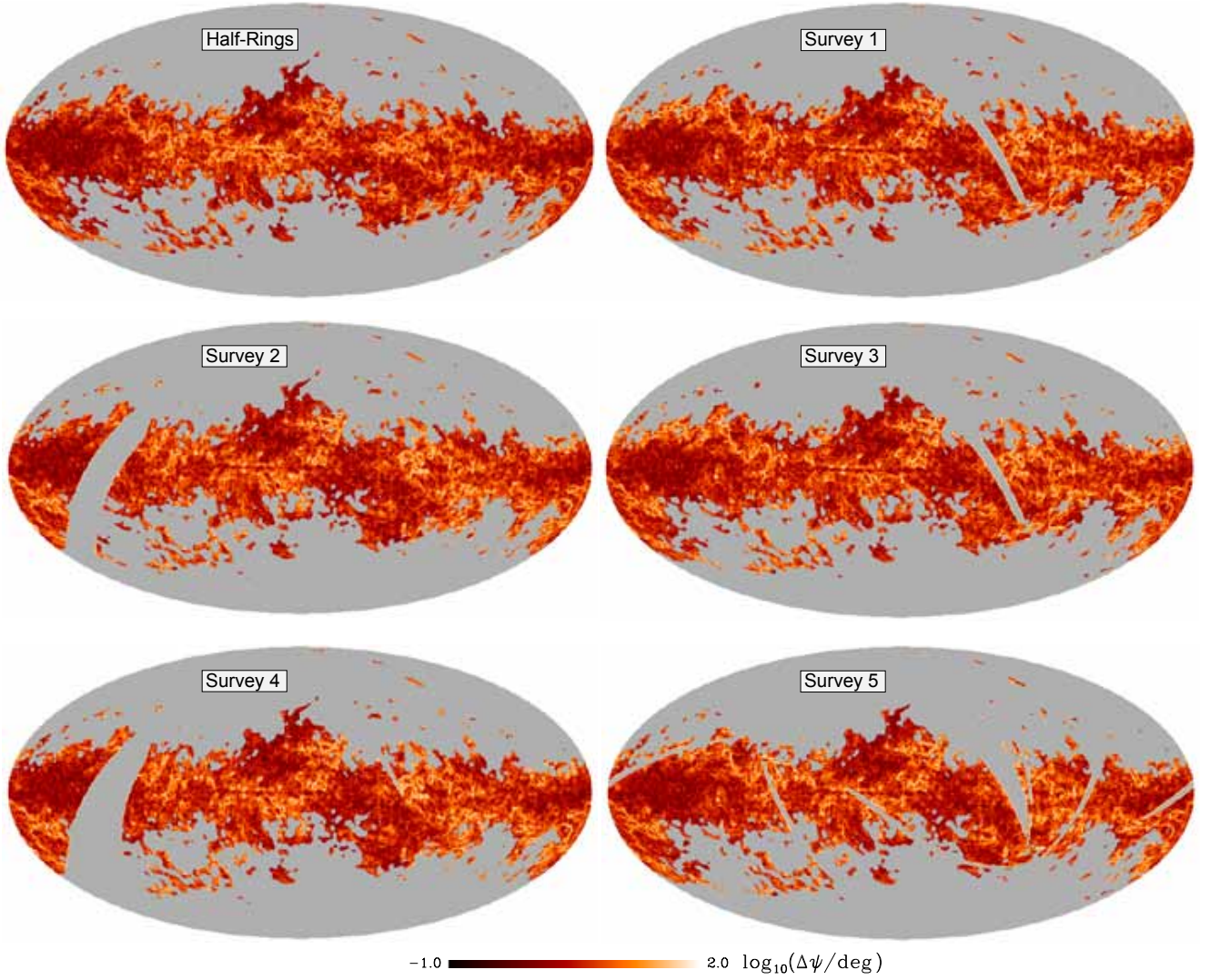


Fig. 12. Maps of the polarization angle dispersion function $\Delta\psi$ computed from half-ring correlations ($\Delta\psi_H$) and for individual *Planck* surveys. The maps are shown with a common \log_{10} scale.

Table 2. Statistics of the percentage polarization fraction p at various data resolutions, θ . The table gives the data resolution (column 1) and the median and maximum values of p (columns 2 and 3). The last column (4) shows the maximum values for $p - 4\sigma_p$. The average value is computed in the last line and used as the value for p_{\max} .

θ	med(p)	max(p)	max($p - 4\sigma_p$)
15'	5.5	81.8	20.3
30'	5.3	48.7	20.0
1°0	5.1	25.6	19.0
Average			$19.8 \pm 0.7\%$

At low f_{sky} values and high resolutions, high values of p are observed. Inspection of the maps indicates that these are point-like objects, either isolated pixels or actual point sources. Since we are interested in diffuse emission only, these isolated values are ignored in evaluating p_{\max} . Table 2 lists the maximum and median values of p at different resolutions. It also shows the

maximum value of $p - 4\sigma_p$ observed at each resolution. We use the average of these values as a conservative estimate of p_{\max} and find $p_{\max} > 19.8\%$. This indicates that, in the most favourable conditions for dust alignment, the intrinsic polarization fraction p_0 is larger than 19.8%.

4.2. Polarization fraction vs column density

We now analyse the variations of the polarization fraction p with dust column density. We use the Bayesian mean posterior estimate of p described in Sect. 2.3 and shown in Fig. 4, computed at 1° resolution. For the dust optical depth map, we use the map of τ_{353} derived in [Planck Collaboration XI \(2014\)](#). The maps were computed at 1° resolution. Following [Planck Collaboration XI \(2014\)](#), we adopt the conversion factor from τ_{353} to A_V or gas column density, derived using the Galactic extinction from measurements of quasars,

$$N_H = (1.41 \times 10^{26} \text{ cm}^{-2}) \tau_{353}, \quad (12)$$

which leads to

$$A_V = 4.15 \times 10^4 \tau_{353}, \quad (13)$$

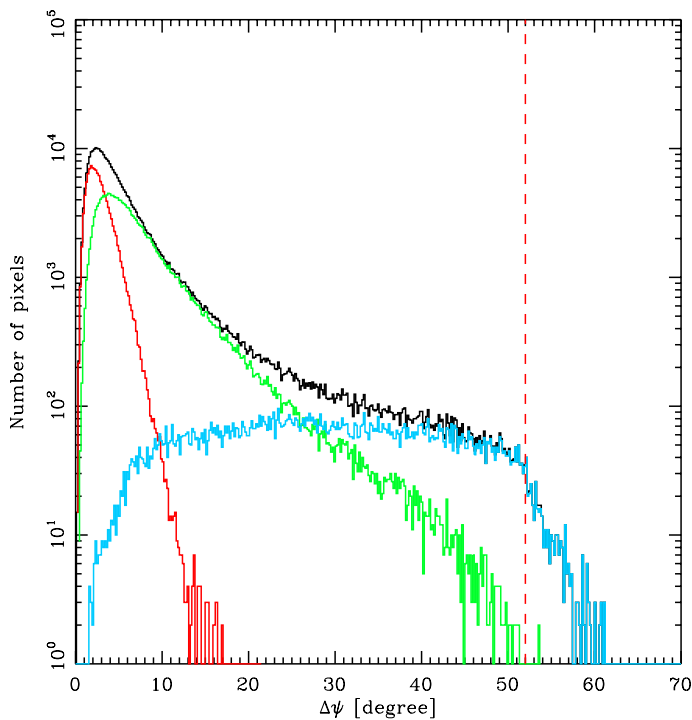


Fig. 13. Histogram of $\Delta\psi$ at 353 GHz at 1° resolution and a lag $\delta = 30'$. The black curve shows the full distribution over the sky area covered in Fig. 11. The red, green, and blue curves show the histograms for regions covered in Fig. 11 with $p > 5\%$, $1\% < p < 5\%$, and $p < 1\%$, respectively. The vertical dashed line shows $\Delta\psi = 52^\circ$, which is the limit for pure random noise on $\Delta\psi$.

when using $R_V=3.1$.

Figure 18 shows the distribution of data for the polarization fraction p as a function of N_H , as derived from dust optical depth, both for the sky fraction shown in Fig. 4 and for the same region but excluding the inner Galactic plane (i.e., excluding $\ell_{\text{II}} < 90^\circ$ or $\ell_{\text{II}} > 270^\circ$, $|b_{\text{II}}| < 2^\circ$). As can be seen in the figure, the plot shows both considerable scatter at a given N_H , and also systematic trends with N_H . The scatter in p is likely due to depolarization in the beam or along the LOS and/or to intrinsic variations in p . Possible origins of this scatter are analysed in Planck Collaboration Int. XX (2014). At low column densities ($2 \times 10^{20} \text{ cm}^{-2} < N_H < 10^{21} \text{ cm}^{-2}$, $0.1 < A_V < 0.5 \text{ mag}$), p values generally remain below $p \approx 15\%$. The maximum p values are reached in this N_H range. We observe an ensemble average polarization of 7% at $N_H = 10^{21} \text{ cm}^{-2}$ ($A_V = 0.5 \text{ mag}$). The average values of p at lower column densities are not discussed in this paper, since a proper treatment would require a careful analysis of the residual bias in the method used to derive p . This will be the subject of a future paper. At larger N_H ($10^{21} \text{ cm}^{-2} < N_H < 2 \times 10^{22} \text{ cm}^{-2}$, $0.5 < A_V < 10 \text{ mag}$), p values are typically below $p \approx 10\%$ and show a steady decline, with $\langle p \rangle$ decreasing down to $\approx 4\%$. We observe a sharp drop in p starting at $N_H \approx 2 \times 10^{22} \text{ cm}^{-2}$ ($A_V \approx 10 \text{ mag}$). Above $N_H \approx 4 \times 10^{22} \text{ cm}^{-2}$ ($A_V \approx 20 \text{ mag}$) values of p are systematically below 4% with an average value of $\langle p \rangle \approx 1\text{--}2\%$.

Towards, nearby dense cores ($n_H > 3 \times 10^4 \text{ cm}^{-3}$, size $\sim 0.1 \text{ pc}$, $N_H > 10^{22} \text{ cm}^{-2}$) the polarization fraction is observed to decrease systematically with N_H . This effect contributes to the sharp drop observed at $2 \times 10^{22} \text{ cm}^{-2}$ (Fig. 18,

bottom panel). Inspection of the *Planck* polarization map at 353 GHz shows many examples of such dips in p associated with nearby dense clouds. A systematic statistical study in the vicinity of *Planck* cold clumps will be presented in a forthcoming paper. Figure 19 shows the example of the dark cloud L134 (Tucker et al. 1976; Mattila et al. 1979) which is located at high Galactic latitude in the otherwise highly polarized Aquila Rift. L134 is one of the coldest Cold Clumps in the *Planck* catalogue (Planck Collaboration XXIII 2011). It is clearly seen that p can be as large as 10% in the external regions and decreases to values as low as 1% at the column density peak. This behaviour appears to be common in the high-latitude sky and confirms previous studies. Such a decrease of the polarization fraction towards large column densities on cloud scales was reported previously in ground-based measurements of polarization both in emission (Ward-Thompson et al. 2000; Matthews & Wilson 2000) and extinction (e.g., Gerakines & Whittet 1995; Whittet et al. 2008). This is usually interpreted as being due to a gradual loss of alignment of dust grains in dense shielded regions. In the likely hypothesis that dust alignment processes involve UV and visible photons spinning up the grains (Draine & Weingartner 1996; Hoang & Lazarian 2008), polarization in externally heated clouds is expected to drop off rapidly when outside UV radiation cannot penetrate them. The gradual decrease of p observed in Fig. 18 above $A_V = 1 \text{ mag}$ is roughly consistent with such a scenario.

However, the decrease of the polarization fraction with increasing column density could also be due to fluctuations in the orientation of the magnetic field along a long LOS, causing depolarization. In order to shed light on this depolarization effect, the companion paper Planck Collaboration Int. XX (2014) compares the polarization properties of the *Planck* dust emission with maps of polarized emission computed in simulations of MHD turbulence. The simulations are anisotropic to allow for an analysis of the influence of a large-scale magnetic field combined with a turbulent field. The polarized dust emission is computed using a uniform dust intrinsic polarization fraction $p_0 = 20\%$. A large scatter in the polarization fraction p per bin of column density and a decrease of the maximum (and mean) values of p with N_H are found in the simulated maps, similar to those observed. Therefore, the variation of p with N_H resembles that inferred from MHD simulations, even though no loss of dust alignment efficiency due to radiative transfer is included. This indicates that the depolarization observed towards dense isolated clumps such as L134 is not necessarily the result of a loss of dust alignment, but could also be due to the tangling of magnetic field lines.

As shown in Fig. 18, which displays the dependence of p on N_H over the whole sky and in regions excluding the inner Galactic plane, most lines of sight with very low p values are within the inner Galactic plane. The large gas column densities in the inner Galaxy ($A_V > 20 \text{ mag}$) arise both in massive star forming regions (i.e., dense gas with $n_H > 3 \times 10^4 \text{ cm}^{-3}$ for regions around 0.3 to 1 pc), but also along long lines of sight (say 10 kpc) sampling mostly low density gas in the Molecular Ring. We argue that the contribution from such star forming regions in the inner Galaxy is small in the *Planck* maps at a resolution of $1'$, because such regions have angular sizes smaller than $1'$ if they are located further than 2 kpc from the Sun. The tail of high column densities in the inner Galaxy is therefore mostly due to long lines of sight sampling low density gas.

For lines of sight towards the inner Galactic plane, the question is whether they are probing a dense cold medium, shielded from the ambient UV field, or if they result from the accumula-

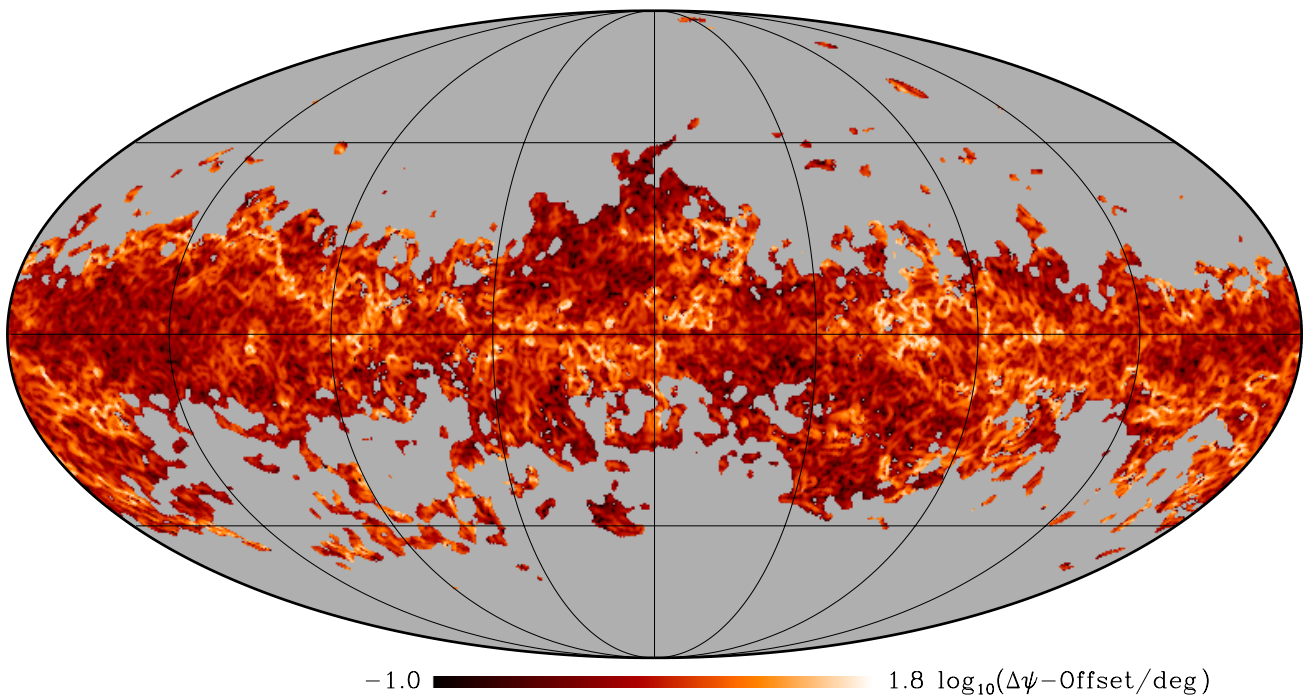


Fig. 14. Same as Fig. 11 but with the noise-induced offset subtracted, as derived from a test with $\Delta\psi = 0^\circ$ (see Appendix C for details).

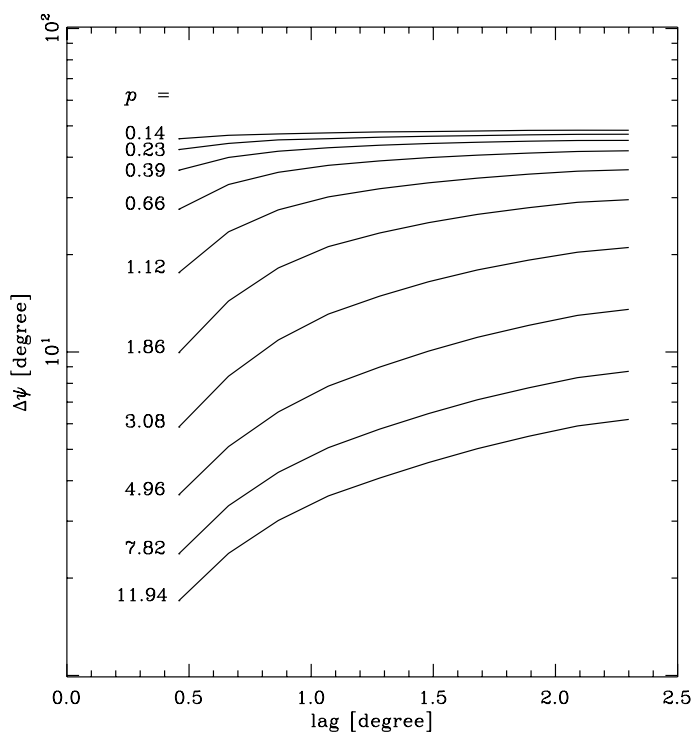


Fig. 15. Evolution of the polarization angle dispersion function ($\Delta\psi$) at 353 GHz as a function of lag δ , binned in intervals of the polarization fraction p . The curves are labelled with the median polarization fraction in the bin as a percentage.

tion of low density material distributed over large distances. The apparent dust temperature can in principle be used to discriminate between these two situations. Figure 20 shows the distribu-

tion of the apparent dust temperature (T_{obs}), as derived from the dust SED fitting in Planck Collaboration XI (2014) using a modified grey-body fit, as a function of column density. As discussed in Planck Collaboration XI (2014) the apparent dust temperature generally decreases with increasing column density, up to $N_{\text{H}} \approx 10^{22} \text{ cm}^{-2}$. The figure shows that, at higher column densities, T_{obs} increases again with N_{H} . The bulk of the large column densities above about $3 \times 10^{22} \text{ cm}^{-2}$ therefore probe material in which dust is warmer than in the cold shielded cores, because it resides either in the low density medium, weakly shielded from the UV field of the inner Galaxy, or close to star-forming regions. In this case, the observed decrease of p is unlikely to be due to radiative transfer effects alone. This is taken as additional evidence that the structure of the magnetic field could be the main interpretation for the apparent decrease of p with column density.

4.3. Polarization fraction vs angle dispersion function

Figure 11 shows the distribution of $\Delta\psi$ computed as described in Sect. 3.3 from the full survey at 353 GHz for 1° resolution and with a $\delta = 30'$ lag used in the analysis.

The map of $\Delta\psi$ exhibits a wide range of values. A striking feature of the map is the existence of confined regions of high $\Delta\psi$ values, often reaching 50° to 70° , which are organized in an intricate network of filamentary structures, some of which span more than 30° in length. Figure 16 shows maps of selected regions around some of these high $\Delta\psi$ regions. Inspection of the polarization maps shows that these filamentary features generally lie at the boundary between regions with uniform, but different, magnetic field orientations on the sky.

Maps computed at larger lags look similar to those shown in Fig. 11, although with wider filamentary features, due to the larger scale of the analysis. Maps computed at smaller lags show filamentary features at the same locations as in Fig. 11, which

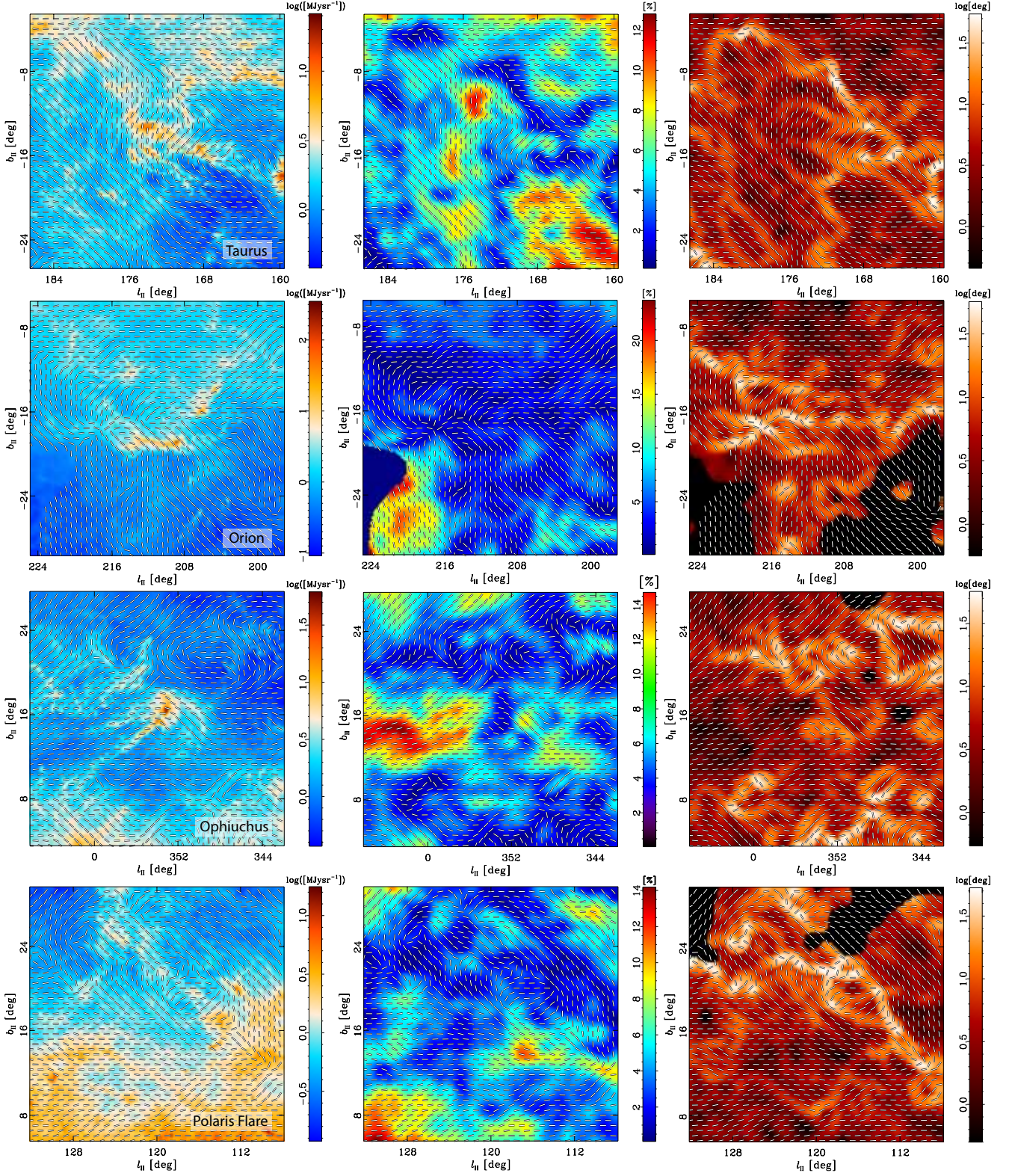


Fig. 16. Maps of a few selected regions, illustrating the relation between polarization fraction and polarization angle dispersion function. *Left:* intensity at 353 GHz. *Centre:* polarization fraction. *Right:* polarization angle dispersion function, $\Delta\psi$, shown in log scale. Regions are from top to bottom: Taurus, Orion, Ophiuchus, and Polaris.

indicates that the structures are in general unresolved. We also derived maps of $\Delta\psi$ at higher resolution. However, the noise and bias on $\Delta\psi$ increase quickly at higher resolution, which makes it impossible to follow the structure of the filamentary features

down to the full *Planck* resolution of $5'$ in most regions of the sky.

Comparison with the observed polarization fraction map of Fig. 4 on large scales clearly shows that, overall, the filamentary

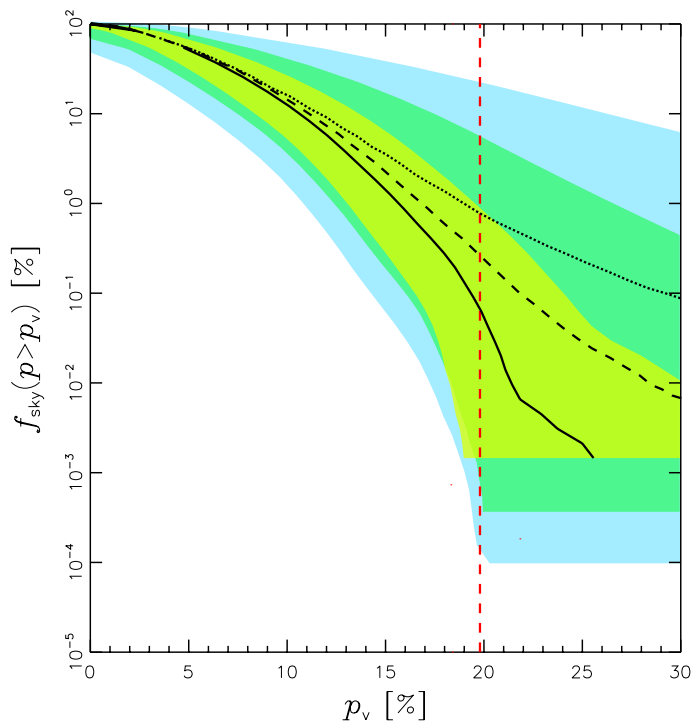


Fig. 17. Fraction of the sky $f_{\text{sky}}(p > p_v)$ above a given polarization fraction value p_v , as a function of p_v at the resolution of 1° (solid line, yellow), $30'$ (dashed line, green), and $15'$ (dotted line, blue). The range shown is the sky fraction corresponding to $p \pm 4\sigma_p > p_v$. The vertical dashed line shows the adopted common value of $p_{\text{max}} = 19.8\%$.

features of high $\Delta\psi$ correspond to low values of p . A similar trend was observed previously in the OMC-2/3 molecular clouds regions by Poidevin et al. (2010), using $14''$ resolution polarimetry data at 353 GHz. The *Planck* large-scale maps show that this is a general trend, as confirmed by the plot in Fig. 21, which shows that p and $\Delta\psi$ are approximately linearly anti-correlated in a log-log plot. Low p regions often correspond to regions where the observed polarization direction ψ changes. This result is in line with the findings of the previous section and further supports the fact that variations in the magnetic field orientation play an important role in lowering the observed polarization fraction. The best-fit correlation shown in Fig. 21 is given by

$$\log_{10}(\Delta\psi) = \alpha \times \log_{10}(p) + \beta, \quad (14)$$

with $\alpha = -0.834$ and $\beta = -0.504$.

The above results are compared with those inferred from MHD simulations in Planck Collaboration Int. XX (2014). The simulations clearly show an anti-correlation between $\Delta\psi$ and p , with a slope similar to that observed in the data. It is worth noting that in the noiseless simulations, the observed trend cannot be produced by the bias on $\Delta\psi$ resulting from higher uncertainties in polarization angles in regions of low signal and/or polarization fraction. It clearly results from averaging effects of the polarization angle within the beam and along the LOS. In brief, field line tangling weakens p , especially when the large-scale field tends to be aligned with the LOS.

The regions of large $\Delta\psi$ bear some resemblance to the so-called “depolarization canals” (e.g., Haverkorn et al. 2000), or more generally the regions of high polarization gradient (Gaensler et al. 2011), detected in maps of radio polarized emis-

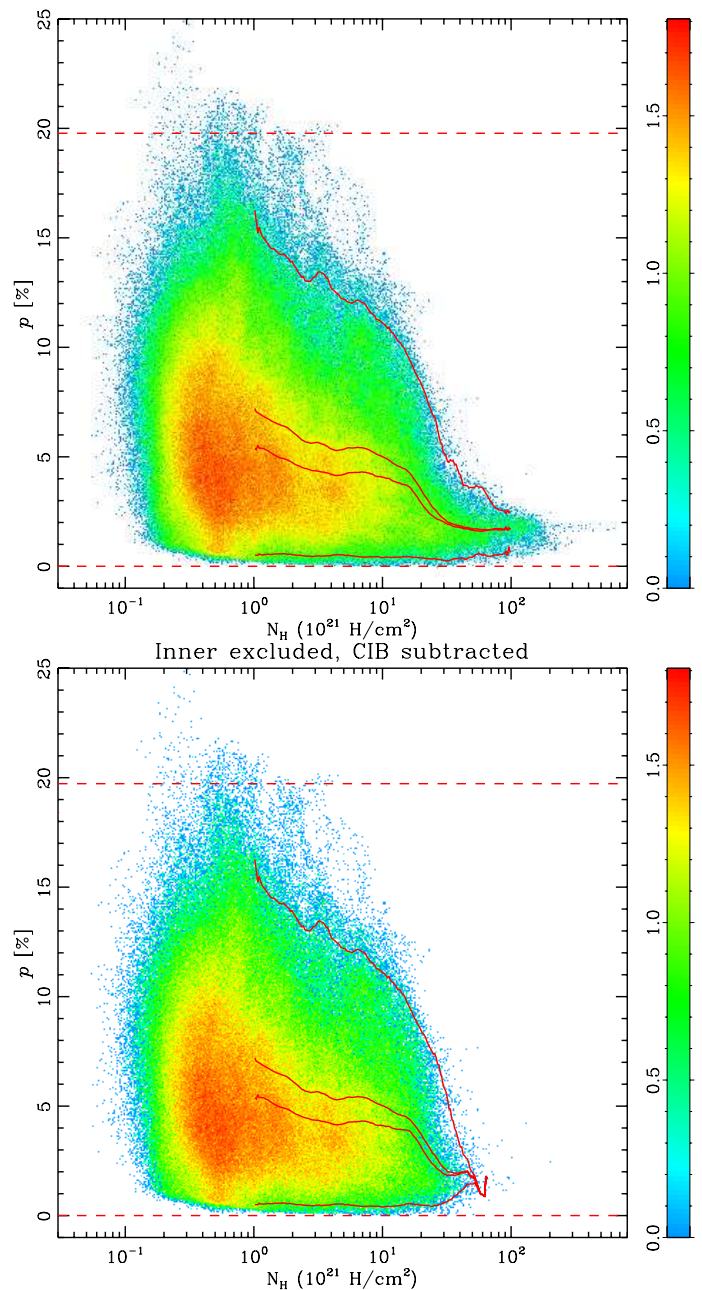


Fig. 18. Distribution of the polarization fraction (p) as a function of gas column density over the whole sky (upper panel) and in regions of the sky excluding the inner Galactic plane (excluding $\ell_{\text{II}} < 90^\circ$ or $\ell_{\text{II}} > 270^\circ$, $|b_{\text{II}}| < 2^\circ$) (lower panel). The values of p were computed at 1° resolution. The gas column density is derived from the dust optical depth at 353 GHz (see text). The colour scale shows the pixel density in \log_{10} scale. The curves show, from top to bottom, the evolution of the upper 1% percentile, mean, median and lower 1% percentile of p for pixels with $N_{\text{H}} > 10^{21} \text{ cm}^{-2}$. Horizontal dashed lines show the location of $p = 0$ and $p_{\text{max}} = 19.8\%$.

sion from the warm ionized medium (WIM). However, the two types of features have different origins. As explained earlier, the filamentary features of large $\Delta\psi$ are generally associated with discontinuities (at the resolution of the observations) in the magnetic field orientation within dust-emitting regions. In contrast, the radio depolarization canals arise from Faraday rotation ef-

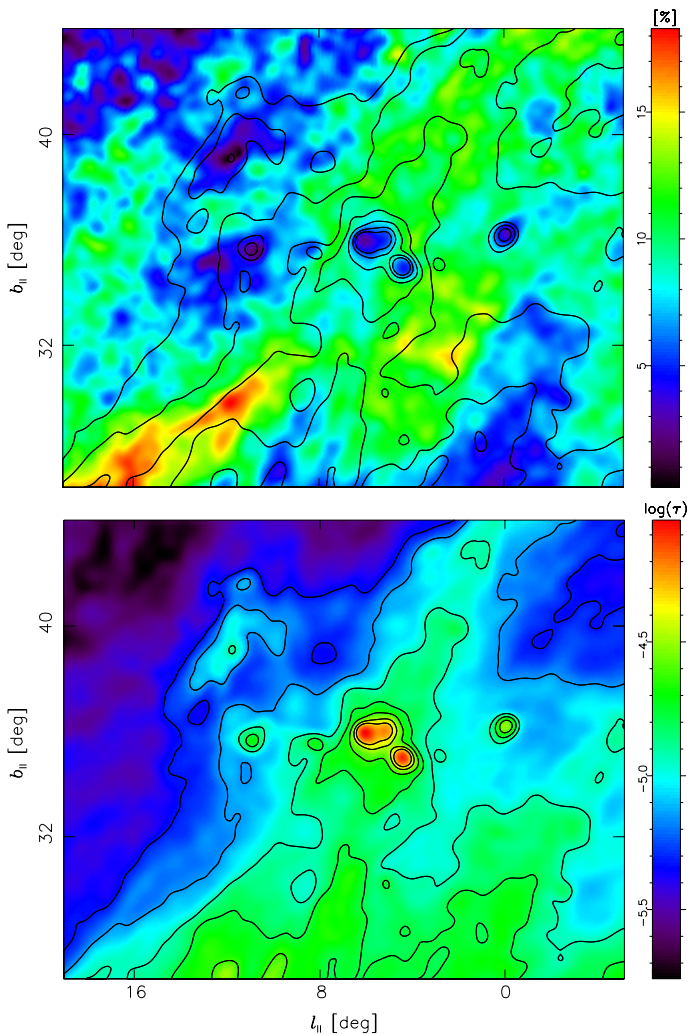


Fig. 19. *Top:* Map of the polarization fraction towards the dark molecular cloud L134, overlaid with contours of the dust optical depth at 353 GHz. The levels are $\tau_{353} = 1.4, 2.9,$ and 5.8×10^{-5} , corresponding to $A_V = 0.6, 1.2,$ and 2.4 mag. *Bottom:* Same for the dust optical depth. The maps are shown at a common resolution of $30'$.

fects: they are thought to be due to either differential Faraday rotation (and hence depolarization) within synchrotron emission regions or discontinuities in foreground Faraday rotation screens (e.g., Fletcher & Shukurov 2007). The first class of depolarization canals do not correspond to true physical structures, and their observed positions in the sky vary with radio frequency. The second class of depolarization canals, and more generally the regions of high radio polarization gradient, are somewhat similar to our filamentary features of large $\Delta\psi$, insofar as both can be traced back to physical discontinuities. But because the physical quantities that undergo a discontinuity (free-electron density and LOS field component for the former *versus* sky-projected field orientation for the latter) as well as the places where the discontinuities occur (foreground Faraday rotation screens for the former *versus* dust-emitting regions for the latter) are unrelated, one does not expect any one-to-one correspondence.

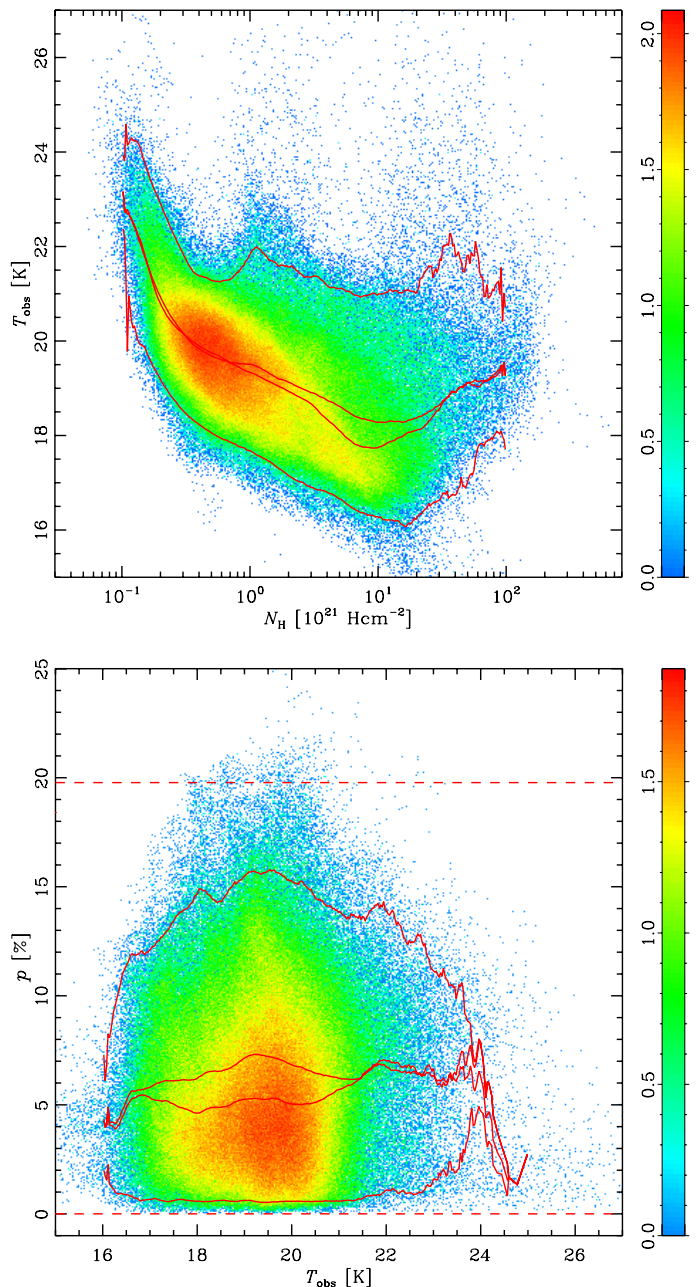


Fig. 20. *Upper:* Distribution of the apparent dust temperature (T_{obs}) and column density, as derived in Planck Collaboration XI (2014). *Lower:* Distribution of the polarization fraction (p) as a function of T_{obs} in regions of the sky excluding the inner Galactic plane (excluding $\ell_{\text{II}} < 90^\circ$ or $\ell_{\text{II}} > 270^\circ$, $|b_{\text{II}}| < 2^\circ$). Both plots are for pixels not masked in Fig. 1. The colour scale shows the pixel density on a \log_{10} scale. The curves show, from top to bottom, the evolution of the upper 1% percentile, mean, median and lower 1% percentile of p . Horizontal dashed lines show the location of $p = 0$ and $p_{\text{max}} = 19.8\%$.

4.4. Dust vs synchrotron polarization

In this section we compare the dust with radio polarization data. Our aim is to test how much the complementary observables trace the same magnetic fields and how their polarization properties are affected by the irregular component of the field. These

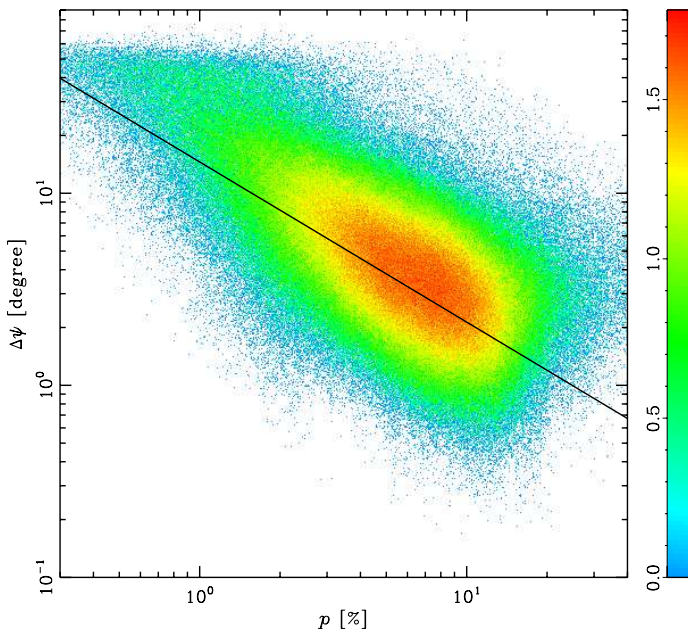


Fig. 21. Scatter plot of the polarization angle dispersion function $\Delta\psi$ as a function of polarization fraction p at 353 GHz. The colour scale shows the pixel density on a \log_{10} scale. The line indicates the best fit (see text).

Table 3. Slope, intercepts and Pearson correlation coefficients of the correlation between dust and synchrotron polarization fraction, computed over Galactic quadrants in the MW plane and off the plane.

Quadrant	$ b_{\text{II}} < 5^\circ$			$ b_{\text{II}} > 5^\circ$		
	Slope	Intercept	Pearson	Slope	Intercept	Pearson
Q1	0.310	-0.551	0.341	0.280	-0.548	0.288
Q2	0.355	-0.379	0.470	0.144	-0.687	0.155
Q3	0.229	-0.646	0.300	0.101	-0.679	0.091
Q4	0.135	-0.835	0.170	0.053	-0.818	0.058
All	0.346	-0.462	0.469	0.137	-0.704	0.144

comparisons tell us not only about the fields but also about the relative distributions of dust grains and relativistic electrons.

The synchrotron and dust emission are both linearly polarized perpendicular to the local sky-projected magnetic field. The emissivities, however, have different dependencies on the magnetic field strength: the dust emission does not depend on the field strength, whereas the synchrotron emissivity is given by $\mathcal{E}_{\text{syn}} \propto n_e B_{\perp}^{(\gamma+1)/2}$, where n_e is the density of relativistic electrons and γ is the power-law index of the relativistic-electron energy spectrum (typically $\gamma \simeq 3$, so that $\mathcal{E}_{\text{syn}} \propto n_e B_{\perp}^2$). One therefore has to be careful in interpreting the comparison between these observables. Some differences arise when the magnetic field in dust clouds differs from that in the diffuse synchrotron-emitting medium. Other differences arise because of the emissivity dependence on the field strength that weights the emission differently along the LOS. Any single direction may have a combination of these effects. We would therefore expect to see globally similar polarization structures where the particles sample the same average field, but not identical structures. A correlation analysis between dust and synchrotron polarization is

also reported by [Planck Collaboration Int. XXII \(2014\)](#). Their cross-correlation between the Q and U maps at *WMAP* and LFI frequencies with the corresponding maps at 353 GHz shows that some of the polarized synchrotron emission at intermediate Galactic latitudes is correlated with dust polarization in both intensity and angle. We might further expect to see statistical correlations even where the irregular component perturbs the large-scale magnetic field, but the degree of the correlation is complicated to predict.

The data sets are described in Sect. 2.5. Figure 22 compares both the polarization fraction and the polarization angle of the dust emission at 353 GHz (the Bayesian estimates where the S/N on p is greater than 3) with polarized synchrotron emission at 30 GHz. The comparison between the polarization angles is straightforward, as synchrotron is dominant and there is no Faraday rotation at these frequencies. The comparison between the polarization fractions is more complex, however, because in the microwave and radio data there are additional total intensity components, such as free-free and anomalous microwave emission. To avoid contamination from anomalous microwave emission, we use the 408 MHz map of [Haslam et al. \(1982\)](#) for synchrotron total intensity. We correct for free-free emission as described in Sect. 2.5. This correction is approximate, but the synchrotron component dominates at low frequencies. We extrapolate the 408 MHz intensity to 30 GHz in order to construct the polarization fraction, assuming a spectral index of -2.88 (see, e.g., [Jaffe et al. 2011](#)). Note that a change in this constant index will simply shift the synchrotron polarization fraction systematically up or down and not affect any observed correlation. Spatial variations in the index that are not accounted for, however, remain a limitation of this simple method.

The left two columns of Fig. 22 show the Galactic plane ($|b_{\text{II}}| < 5^\circ$), while the right two show the results for the rest of the sky. The correlations are quantified by linear fits and Pearson’s correlation coefficients listed in Table 3. In all but the fourth quadrant, there is clear correlation in the polarization fraction in the plane, where the polarized intensity is strong. The polarization angles remain near zero, i.e., the magnetic field remains largely parallel to the plane. This confirms that at the largest scales probed through the full disk, the synchrotron and dust sample roughly the same average magnetic fields. With a few notable exceptions, however, there is little correlation away from the plane, where isolated local structures and the irregular field component become more important.

The so-called Fan region in the second quadrant is one where the comparison is most interesting, showing a relatively strong correlation ($r = 0.47$) in polarization fraction in the plane, as does the third quadrant to a lesser degree. Out of the Galactic plane, the correlation in p disappears. But we still see correlation in the polarization angles off the plane, where they remain concentrated around zero, i.e., perpendicular to the plane, indicating that the magnetic field is parallel to the plane even at latitudes above 5° . The second interesting region for the comparison is the first quadrant, where the sky is dominated by the radio loop I, i.e., the North Polar Spur (NPS). Here the high-latitude polarization angles show correlation where the two observables clearly trace the same magnetic fields.

We also compare the dust polarization angle dispersion with the polarized synchrotron emission at 1.4 GHz where it is subject to significant Faraday rotation effects. In Fig. 1 of [Burigana et al. \(2006\)](#), the polarization fraction shows strong depolarization of the synchrotron emission within 30° of the plane, with the exception of the Fan region in the second quadrant. Much of the depolarization is so-called “beam depolarization”.

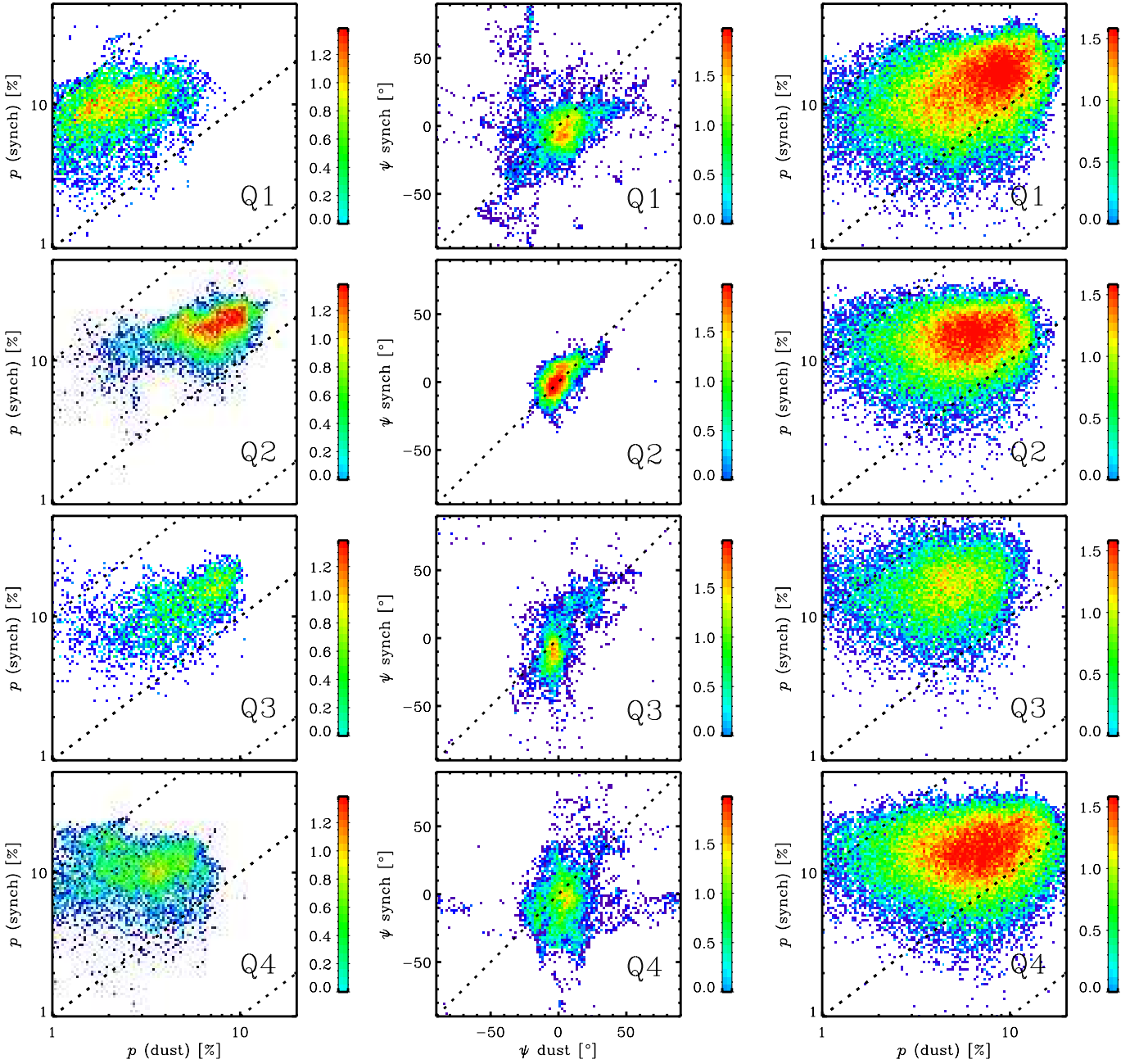


Fig. 22. Comparison of dust and synchrotron polarization fraction and polarization angle for $|b_{\text{II}}| < 5^\circ$ (left panels) and off of the plane for $|b_{\text{II}}| > 5^\circ$ (right panels), separated in the four Galactic quadrants (top to bottom). The colour scale shows the pixel density on a \log_{10} scale.

Even a coherent diffuse background source viewed through the roughly 1° beam results in emission co-added along slightly different lines of sight that pass through different turbulent cells, get Faraday-rotated differently, and cancel out. One might then expect that the resulting synchrotron polarization fraction would anti-correlate with the dust polarization angle dispersion. Lines of sight toward highly turbulent regions should have low synchrotron polarization due to Faraday effects and high dust polarization angular dispersion. Such correlations are not generally apparent, however in some regions, such as the second quadrant dominated by the Fan region, we see this effect, implying that the dust and synchrotron in the Fan are tracing some of the same turbulent magnetic fields.

Finally, it is instructive to compare the dust polarization fraction with Faraday RMs of extragalactic sources using the catalogues of Brown et al. (2003), Brown et al. (2007), Taylor et al. (2009), and Van Eck et al. (2011). We compare the RM of each source with the polarized emission in the corresponding map pixel as shown in Fig. 23. Remember that RMs are proportional to the LOS field component (which is positive/negative if the field points towards/away from the observer) times the free-electron density and integrated along the LOS, whereas the dust polarization fraction is an increasing function of the inclination angle of the magnetic field to the LOS. Therefore, if the large-scale field is reasonably coherent along the LOS path through the Galaxy, then a field orientation globally close to the LOS

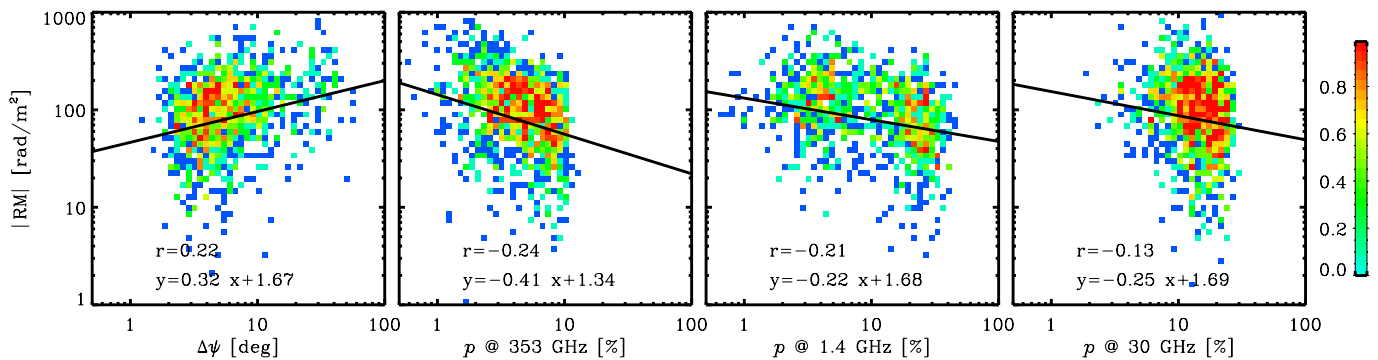


Fig. 23. Faraday RMs in the Galactic plane ($|b_{\text{II}}| < 5^\circ$) compared to (*left to right*): dust angle dispersion; dust polarization fraction at 353 GHz; synchrotron polarization fraction at 1.4 GHz; and synchrotron polarization fraction at 30 GHz. The overplotted lines show the result of a simple linear fit between the two datasets, with the Pearson's r giving the measure of the degree of correlation. The colour scale shows the pixel density on a \log_{10} scale.

will tend to make extragalactic-source RMs large (in absolute values) and the dust polarization fraction small, whereas a field orientation globally close to the plane of the sky will do the opposite. As a result, one might expect a rough anti-correlation between extragalactic-source RMs and dust polarization fraction. However, only a very loose anti-correlation may be expected at best, since: (1) Faraday rotation and dust emission take place in different environments, with possibly different magnetic field directions; (2) RMs depend not only on the field inclination to the LOS, but also on the total field strength and on the free-electron column density; and (3) the LOS field component could undergo reversals, which would decrease RMs without correspondingly increasing the dust polarization fraction. Similarly, one might expect a rough positive correlation between extragalactic-source RMs (again in absolute values) and dust polarization angle dispersion, because if the large-scale field is globally oriented closer to the LOS, the dust polarization angle will be more sensitive to the fluctuating field. Figure 23 confirms these expected trends in the Galactic plane, which traces the large-scale field. Away from the plane (not shown) where more local structures dominate, we find no correlations.

The *Planck* polarization data at 353 GHz provide a new tracer of magnetic fields and an important complement to radio observations due to the independent source particle distribution. This first look at the comparison of these observables confirms the expected large-scale correspondence as well as interesting correlations in the Fan and NPS regions. We find only weak correlations over much of the sky where the effects of local structures and the irregular field component dominate. This fact is not surprising but nonetheless has important implications. Though it is premature to draw physical conclusions from these comparisons, they highlight the importance of, as well as the challenges inherent in combining these data to form a coherent picture of the Galactic magnetic fields.

5. Conclusions

We have presented the *Planck* large-scale polarization maps at 353 GHz, where polarization is dominated by polarized thermal dust emission from elongated grains aligned with the magnetic field. These data allow us for the first time to study dust polarization over large angular scales and opens the field for many detailed studies to come.

The dust polarization fraction p is observed to range from zero to more than 15%. We derive a lower limit to the maximum

polarization fraction of $p_{\text{max}} = 19.8\%$. These highest polarization fractions are observed in a handful of individual regions, usually located in intermediate to low column density parts of the sky.

The large-scale spatial distribution of p shows a modulation that is consistent with predictions of the general magnetic field structure of the MW, as constrained previously from synchrotron and RM data. At smaller scales, the variations of p appear to be related to variations in both the total dust column density and the magnetic field structure.

There is a clear tendency for p to decrease with total column density. The variations associated with column density show that p starts to drop below around $A_V = 1$ mag and show a sharp drop above $A_V = 10$ mag. This is qualitatively consistent with the prediction of models where dust alignment results from the interaction with light. However, tangling of the \mathbf{B} field geometry along the LOS is also very effective at suppressing the net polarization fraction and possibly plays the major role in most cases, as discussed in [Planck Collaboration Int. XX \(2014\)](#).

The *Planck* polarization data at 353 GHz also allow precise measurements of the polarization direction ψ over most of the sky. Rotated by 90° , this direction is assumed to represent the \mathbf{B} -field orientation projected on the sky. The polarization angles in the Galactic plane are observed to be consistent with the expectation that \mathbf{B} lies mostly along the plane, as strongly suggested by previous synchrotron measurements. This is particularly true in the inner MW and in the highly polarized Fan region.

In order to characterize the field rotation, we use the polarization angle dispersion function $\Delta\psi$, which measures the dispersion in angle rotation at a given spatial scale. $\Delta\psi$ increases with lag distance, as previous observations have shown at smaller scales in specific regions. Away from the Galactic plane, the sky distribution of $\Delta\psi$ reveals a spectacular complex of unresolved filamentary structures of large $\Delta\psi$ values. This is the first time such structures have been observed for dust polarization. These filamentary structures anti-correlate with p , in the sense that regions with maximal rotation generally correspond to the lowest polarization fractions. We demonstrate that, over a large fraction of the sky, this is not due to the noise-induced bias on $\Delta\psi$ and is therefore a real effect.

We interpret the anti-correlation between $\Delta\psi$ and p as depolarization due to the magnetic field structure. This is likely produced by field rotation both in the plane of the sky below the resolution of the data and along the LOS. The filamentary structures often appear to be separating adjacent regions that have

different but quite homogeneous field orientations. When they can be followed down to the *Planck* resolution, their widths are smaller than the beam. Some of them span large angular distances at high latitudes, which suggests that they are local. The filamentary structures bear a resemblance to the depolarization canals that are observed at radio frequencies and attributed to Faraday rotation effects, but we argue that they have a different origin here. The regions of high $\Delta\psi$ are also observed in MHD simulations (see details in [Planck Collaboration Int. XX 2014](#)), with the same type of anti-correlation with p as that observed in the *Planck* data. This similarity provides further support for the above interpretation.

We compared the dust polarization fraction and angle with polarized synchrotron data. There are clear indications that the two tracers globally see the same magnetic field orientation, particularly interesting to see in the Fan region and the North Polar Spur, but that the detailed distributions of dust and high-energy electrons must be different in order to explain the observed maps. We infer a loose statistical correlation between extragalactic-source RMs and both the dust polarization fraction p and the angle dispersion function $\Delta\psi$. However, inspection of the maps shows that there is no systematic spatial correspondence between depolarization filamentary structures in dust and synchrotron emission at small angular scales.

Acknowledgements. The development of *Planck* has been supported by: ESA; CNES and CNRS/INSU-IN2P3-INP (France); ASI, CNR, and INAF (Italy); NASA and DoE (USA); STFC and UKSA (UK); CSIC, MICINN, JA, and RES (Spain); Tekes, AoF, and CSC (Finland); DLR and MPG (Germany); CSA (Canada); DTU Space (Denmark); SER/SSO (Switzerland); RCN (Norway); SFI (Ireland); FCT/MCTES (Portugal); and PRACE (EU). A description of the *Planck* Collaboration and a list of its members, including the technical or scientific activities in which they have been involved, can be found at http://www.sciops.esa.int/index.php?project=planck&page=Planck_Collaboration. We acknowledge the use of the Legacy Archive for Microwave Background Data Analysis (LAMBDA), part of the High Energy Astrophysics Science Archive Center (HEASARC). HEASARC/LAMBDA is a service of the Astrophysics Science Division at the NASA Goddard Space Flight Center. Some of the results in this paper have been derived using the HEALPix package.

References

- Alves, M. I. R., Davies, R. D., Dickinson, C., et al. 2010, *MNRAS*, 405, 1654
- Beck, R. 2009, in *IAU Symposium*, Vol. 259, *IAU Symposium*, ed. K. G. Strassmeier, A. G. Kosovichev, & J. E. Beckman, 3–14
- Bennett, C. L., Larson, D., Weiland, J. L., et al. 2013, *ApJS*, 208, 20
- Benoît, A., Ade, P., Amblard, A., et al. 2004, *A&A*, 424, 571
- Berkhuijsen, E. M. 1971, *A&A*, 14, 359
- Bersanelli, M., Mandolesi, N., Butler, R. C., et al. 2010, *A&A*, 520, A4
- Brown, J. C., Haverkorn, M., Gaensler, B. M., et al. 2007, *ApJ*, 663, 258
- Brown, J. C., Taylor, A. R., & Jackel, B. J. 2003, *ApJS*, 145, 213
- Burigana, C., La Porta, L., Reich, P., & Reich, W. 2006, *Astron. Nachr.*, 327, 491
- Curran, R. L. & Chrysostomou, A. 2007, *MNRAS*, 382, 699
- Davis, Jr., L. & Greenstein, J. L. 1951, *ApJ*, 114, 206
- Delabrouille, J., Betoule, M., Melin, J.-B., et al. 2013, *A&A*, 553, A96
- Dolginov, A. Z. & Mitrofanov, I. G. 1976, *Ap&SS*, 43, 291
- Dotson, J. L., Davidson, J., Dowell, C. D., Schleuning, D. A., & Hildebrand, R. H. 2000, *ApJS*, 128, 335
- Dotson, J. L., Vaillancourt, J. E., Kirby, L., et al. 2010, *ApJS*, 186, 406
- Draine, B. T. & Fraise, A. A. 2009, *ApJ*, 696, 1
- Draine, B. T. & Weingartner, J. C. 1996, *ApJ*, 470, 551
- Draine, B. T. & Weingartner, J. C. 1997, *ApJ*, 480, 633
- Dunkley, J., Komatsu, E., Nolta, M. R., et al. 2009, *ApJS*, 180, 306
- Falceta-Gonçalves, D., Lazarian, A., & Kowal, G. 2008, *ApJ*, 679, 537
- Fauvet, L., Macías-Pérez, J. F., Aumont, J., et al. 2011, *A&A*, 526, A145
- Fauvet, L., Macías-Pérez, J. F., & Désert, F. X. 2012, *Astroparticle Physics*, 36, 57
- Fauvet, L., Macías-Pérez, J. F., Hildebrandt, S. R., & Désert, F.-X. 2013, *Advances in Astronomy*, 2013
- Ferrière, K. 2011, *Mem. Soc. Astron. Italiana*, 82, 824
- Fletcher, A. & Shukurov, A. 2007, in *EAS Publications Series*, Vol. 23, *EAS Publications Series*, ed. M.-A. Miville-Deschênes & F. Boulanger, 109–128
- Fraise, A. A., Brown, J.-A. C., Dobler, G., et al. 2009, in *American Institute of Physics Conference Series*, Vol. 1141, *American Institute of Physics Conference Series*, ed. S. Dodelson, D. Baumann, A. Cooray, J. Dunkley, A. Fraise, M. G. Jackson, A. Kogut, L. Krauss, M. Zaldarriaga, & K. Smith, 265–310
- Franco, G. A. P., Alves, F. O., & Girart, J. 2010, *ApJ*, 723, 146
- Gaensler, B. M., Haverkorn, M., Burkhart, B., et al. 2011, *Nature*, 478, 214
- Gaensler, B. M. & Johnston, S. 1995, *MNRAS*, 277, 1243
- Gerakines, P. A. & Whittet, D. C. B. 1995, *Planet. Space Sci.*, 43, 1325
- Gold, B., Odegard, N., Weiland, J. L., et al. 2011, *ApJS*, 192, 15
- Górski, K. M., Hivon, E., Banday, A. J., et al. 2005, *ApJ*, 622, 759
- Hamaker, J. P. & Bregman, J. D. 1996, *A&AS*, 117, 161
- Haslam, C. G. T., Stoffel, H., Salter, C. J., & Wilson, W. E. 1982, *A&AS*, 47, 1
- Haverkorn, M., Brown, J. C., Gaensler, B. M., & McClure-Griffiths, N. M. 2008, *ApJ*, 680, 362
- Haverkorn, M., Katgert, P., & de Bruyn, A. G. 2000, *A&A*, 356, L13
- Hildebrand, R. H., Kirby, L., Dotson, J. L., Houde, M., & Vaillancourt, J. E. 2009, *ApJ*, 696, 567
- Hoang, T. & Lazarian, A. 2008, *MNRAS*, 388, 117
- Jaffe, T. R., Banday, A. J., Leahy, J. P., Leach, S., & Strong, A. W. 2011, *MNRAS*, 416, 1152
- Jaffe, T. R., Leahy, J. P., Banday, A. J., et al. 2010, *MNRAS*, 401, 1013
- Jansson, R. & Farrar, G. R. 2012a, *ApJ*, 757, 14
- Jansson, R. & Farrar, G. R. 2012b, *ApJ*, 761, L11
- Keegstra, P. B., Smoot, G. F., Gorski, K. M., Hinshaw, G., & Tenorio, L. 1997, *Astronomical Data Analysis Software and Systems VI*, 125, 198
- Kobulnicky, H. A., Molnar, L. A., & Jones, T. J. 1994, *AJ*, 107, 1433
- Kovac, J., Leitch, E., Pryke, C., et al. 2002, *Nature*, 420, 772
- Lamarre, J., Puget, J., Ade, P. A. R., et al. 2010, *A&A*, 520, A9
- Lazarian, A. 2003, *J. Quant. Spec. Radiat. Transf.*, 79, 881
- Lazarian, A. 2007, *J. Quant. Spec. Radiat. Transf.*, 106, 225
- Lazarian, A. & Hoang, T. 2007, *MNRAS*, 378, 910
- Magalhães, A. M., Pereyra, A., Melgarejo, R., et al. 2005, in *Astronomical Society of the Pacific Conference Series*, Vol. 343, *Astronomical Polarimetry: Current Status and Future Directions*, ed. A. Adamson, C. Aspin, C. Davis, & T. Fujiyoshi, 305
- Martin, P. G. 1971, *MNRAS*, 153, 279
- Martin, P. G. 2007, in *EAS Publications Series*, Vol. 23, *EAS Publications Series*, ed. M.-A. Miville-Deschênes & F. Boulanger, 165–188
- Matthews, B. C., McPhee, C. A., Fissel, L. M., & Curran, R. L. 2009, *ApJS*, 182, 143
- Matthews, B. C. & Wilson, C. D. 2000, *ApJ*, 531, 868
- Mattila, K., Winnberg, A., & Grasshoff, M. 1979, *A&A*, 78, 275
- Mennella, A., Butler, R. C., Curto, A., et al. 2011, *A&A*, 536, A3
- Page, L., Hinshaw, G., Komatsu, E., et al. 2007, *ApJS*, 170, 335
- Paradis, D., Dobashi, K., Shimoikura, T., et al. 2012, *A&A*, 543, A103
- Pelkonen, V.-M., Juvela, M., & Padoan, P. 2009, *A&A*, 502, 833
- Planck HFI Core Team. 2011, *A&A*, 536, A4
- Planck Collaboration XIX. 2011, *A&A*, 536, A19
- Planck Collaboration XXIII. 2011, *A&A*, 536, A23
- Planck Collaboration I. 2014, *A&A*, in press
- Planck Collaboration II. 2014, *A&A*, in press
- Planck Collaboration III. 2014, *A&A*, in press
- Planck Collaboration IV. 2014, *A&A*, in press
- Planck Collaboration V. 2014, *A&A*, in press
- Planck Collaboration VI. 2014, *A&A*, in press
- Planck Collaboration VII. 2014, *A&A*, in press
- Planck Collaboration VIII. 2014, *A&A*, in press
- Planck Collaboration IX. 2014, *A&A*, in press
- Planck Collaboration X. 2014, *A&A*, in press
- Planck Collaboration XI. 2014, *A&A*, in press
- Planck Collaboration XIV. 2014, *A&A*, in press
- Planck Collaboration XVI. 2014, *A&A*, in press
- Planck Collaboration Int. XX. 2014, *A&A*, submitted, [arXiv:astro-ph/14xx.xxxx]
- Planck Collaboration Int. XXI. 2014, *A&A*, submitted, [arXiv:astro-ph/14xx.xxxx]
- Planck Collaboration Int. XXII. 2014, *A&A*, submitted, [arXiv:astro-ph/1405.xxxx]
- Planck Collaboration Int. XXIII. 2014, *A&A*, to be submitted, [arXiv:astro-ph/14xx.xxxx]
- Poidevin, F., Bastien, P., & Matthews, B. C. 2010, *ApJ*, 716, 893
- Poidevin, F., Falceta-Gonçalves, D., Kowal, G., de Gouveia Dal Pino, E., & Mário Magalhães, A. 2013, *ApJ*, 777, 112
- Ponthieu, N., Macías-Pérez, J. F., Tristram, M., et al. 2005, *A&A*, 444, 327

- Pshirkov, M. S., Tinyakov, P. G., Kronberg, P. P., & Newton-McGee, K. J. 2011, *ApJ*, 738, 192
- Quinn, J. L. 2012, *A&A*, 538, A65
- Reich, P. & Reich, W. 1986, *A&AS*, 63, 205
- Reich, P., Reich, W., & Testori, J. C. 2004, in *The Magnetized Interstellar Medium*, ed. B. Uyaniker, W. Reich, & R. Wielebinski, 63–68
- Reich, P., Testori, J. C., & Reich, W. 2001, *A&A*, 376, 861
- Reich, W. 1982, *A&AS*, 48, 219
- Ruiz-Granados, B., Rubiño-Martín, J. A., & Battaner, E. 2010, *A&A*, 522, A73
- Serkowski, K. 1958, *Acta Astron.*, 8, 135
- Stein, W. 1966, *ApJ*, 144, 318
- Sun, X.-H. & Reich, W. 2010, *Research in Astronomy and Astrophysics*, 10, 1287
- Sun, X. H., Reich, W., Waelkens, A., & Enßlin, T. A. 2008, *A&A*, 477, 573
- Taylor, A. R., Stil, J. M., & Sunstrum, C. 2009, *ApJ*, 702, 1230
- Tegmark, M. & de Oliveira-Costa, A. 2001, *Physical Review D (Particles)*, 64, 63001
- Tucci, M., Martínez-González, E., Vielva, P., & Delabrouille, J. 2005, *MNRAS*, 360, 935
- Tucker, K. D., Dickman, R., & Encrenaz, P. 1976, *ApJ*, 210, 679
- Vaillancourt, J. E. 2007, in *EAS Publications Series*, Vol. 23, EAS Publications Series, ed. M.-A. Miville-Deschênes & F. Boulanger, 147–164
- Van Eck, C. L., Brown, J. C., Stil, J. M., et al. 2011, *ApJ*, 728, 97
- Ward-Thompson, D., Kirk, J. M., Crutcher, R. M., et al. 2000, *ApJ*, 537, L135
- Whittet, D. C. B., Hough, J. H., Lazarian, A., & Hoang, T. 2008, *ApJ*, 674, 304
- Wolleben, M., Fletcher, A., Landecker, T. L., et al. 2010a, *ApJ*, 724, L48
- Wolleben, M., Landecker, T. L., Hovey, G. J., et al. 2010b, *AJ*, 139, 1681

Appendix A: Noise estimates for *Planck* smoothed maps

Here, we show how to smooth polarization maps and derive the covariance matrix associated to the smoothed maps.

A.1. Analytical expressions for smoothing maps of the Stokes parameters and noise covariance matrices

Smoothing intensity maps is straightforward, but this is not the case for polarization maps. In principle, as the polarization frame rotates from one centre pixel to a neighbouring one that will be included in the smoothing, the (Q, U) doublet must be also rotated at the same time (e.g., Keegstra et al. 1997). The issue is similar for evaluating the effects of smoothing on the 3×3 noise covariance matrix, though with mathematically distinct results. In this Appendix, we present an exact analytical solution to the local smoothing of maps of the Stokes I , Q , and U , as well as the effects of smoothing on their corresponding noise covariance matrix.

A.1.1. Smoothing of Stokes parameters

Fig. A.1 presents the geometry of the problem. Let us consider a HEALPix pixel j at point J on the celestial sphere, with spherical coordinates (φ_j, θ_j) . To perform smoothing around this position with a Gaussian beam with standard deviation $\sigma_{1/2} = \text{FWHM}/2.35$ centred at the position of this pixel we select all HEALPix pixels that fall within 5 times the FWHM of the smoothing beam (this footprint is sufficient for all practical purposes). Let k be one such pixel, centred at the point K with coordinates (φ_k, θ_k) , at angular distance β from J defined by

$$\cos \beta = \cos \theta_j \cos \theta_k + \sin \theta_j \sin \theta_k \cos(\varphi_k - \varphi_j). \quad (\text{A.1})$$

The normalized Gaussian weight is then

$$w_k = \frac{e^{-(\beta/\sigma_{1/2})^2/2}}{\sum_i e^{-(\beta/\sigma_{1/2})^2/2}}, \quad (\text{A.2})$$

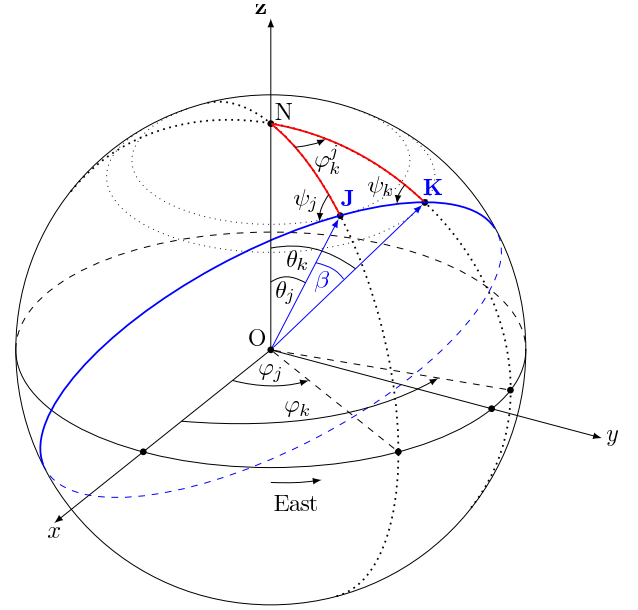


Fig. A.1. Definition of points and angles on the sphere involved in the geometry of the smoothing of polarization maps (adapted from Keegstra et al. 1997). J is the position of the centre of the smoothing beam, and K a neighbouring pixel, with spherical coordinates (φ_j, θ_j) and (φ_k, θ_k) , respectively. The great circle passing through J and K is shown in blue. The position angles ψ_j and ψ_k are in the HEALPix convention, increasing from north through west on the celestial sphere as seen by the observer at O.

and $\sum_k w_k = 1$. Before averaging in the Gaussian beam, we need to rotate the polarization reference frame in K so as align it with that in J. For that the reference frame is first rotated by ψ_k into the great circle running through K and J, then translated to J, and finally rotated through $-\psi_j$. The net rotation angle of the reference frame from point K to point J is then

$$\psi_k^j = \psi_k - \psi_j. \quad (\text{A.3})$$

Due to the cylindrical symmetry around axis z , evaluating ψ_k^j does not depend on the longitudes φ_j and φ_k taken separately, but only on their difference

$$\varphi_k^j = \varphi_k - \varphi_j. \quad (\text{A.4})$$

Using spherical trigonometry in Fig. A.1 with the HEALPix convention for angles ψ_j and ψ_k , we find:

$$\sin \psi_j = \sin \theta_k \sin \varphi_k^j / \sin \beta; \quad (\text{A.5})$$

$$\sin \psi_k = \sin \theta_j \sin \varphi_k^j / \sin \beta; \quad (\text{A.6})$$

$$\cos \psi_j = -(\cos \theta_k \sin \theta_j - \cos \theta_j \sin \theta_k \cos \varphi_k^j) / \sin \beta; \quad (\text{A.7})$$

$$\cos \psi_k = (\cos \theta_j \sin \theta_k - \cos \theta_k \sin \theta_j \cos \varphi_k^j) / \sin \beta. \quad (\text{A.8})$$

To derive ψ_k and ψ_j we use the two-parameter arctan function that resolves the π ambiguity in angles:

$$\psi_k^j = \arctan(\sin \psi_k, \cos \psi_k) - \arctan(\sin \psi_j, \cos \psi_j). \quad (\text{A.9})$$

Because of the tan implicitly used, $\sin \beta$ (a positive quantity) is eliminated in the evaluation of ψ_j , ψ_k , and ψ_k^j .

We can now proceed to the rotation. It is equivalent to rotate the polarization frame at point K by the angle ψ_k^j , or to rotate the

data triplet (I_k, Q_k, U_k) at point K by an angle $-2\psi_k^j$ around the axis I . The latter is done with the rotation matrix (e.g., Tegmark & de Oliveira-Costa 2001)

$$[\mathbf{R}]_k = \begin{bmatrix} 1 & 0 & 0 \\ 0 & \cos 2\psi_k^j & \sin 2\psi_k^j \\ 0 & -\sin 2\psi_k^j & \cos 2\psi_k^j \end{bmatrix}. \quad (\text{A.10})$$

Finally, the smoothed I , Q , and U maps are calculated by:

$$\begin{pmatrix} I \\ Q \\ U \end{pmatrix}_j = \sum_k w_k [\mathbf{R}]_k \begin{pmatrix} I \\ Q \\ U \end{pmatrix}_k. \quad (\text{A.11})$$

A.1.2. Computing the noise covariance matrix for smoothed polarization maps

We want to compute the noise covariance matrix $[\mathcal{C}]_j$ at the position of a HEALPix pixel j for the smoothed polarization maps, given the noise covariance matrix $[\mathbf{C}]$ at the higher resolution of the original data. We will assume that the noise in different pixels is uncorrelated. From the given covariance matrix $[\mathbf{C}]_k$ at any pixel k we can produce random realizations of Gaussian noise through the Cholesky decomposition of the covariance matrix:

$$[\mathbf{C}]_k = [\mathbf{L}]_k \times [\mathbf{L}]_k^T, \quad (\text{A.12})$$

$$(\mathbf{N})_k = [\mathbf{L}]_k \times (\mathbf{G})_k, \quad (\text{A.13})$$

where in the decomposition $[\mathbf{L}]_k^T$ is the transpose of the matrix $[\mathbf{L}]_k$ and $(\mathbf{G})_k = (G_I, G_Q, G_U)_k$ is a vector of normal Gaussian variables for I , Q , and U .

Applying Eq. A.11 to the Gaussian noise realization, we obtain

$$(\mathbf{N})_j = \sum_k w_k [\mathbf{R}]_k \begin{pmatrix} N_I \\ N_Q \\ N_U \end{pmatrix}_k = \sum_k w_k [\mathbf{R}]_k (\mathbf{N})_k. \quad (\text{A.14})$$

The covariance matrix of the smoothed maps at the position J is given by

$$\begin{aligned} [\mathcal{C}]_j &= \langle (\mathbf{N})_j (\mathbf{N})_j^T \rangle \\ &= \left\langle \sum_k w_k [\mathbf{R}]_k [\mathbf{L}]_k (\mathbf{G})_k \sum_i w_i (\mathbf{G})_i^T [\mathbf{L}]_i^T [\mathbf{R}]_i^T \right\rangle \\ &= \sum_{k,i} w_k [\mathbf{R}]_k [\mathbf{L}]_k \langle (\mathbf{G})_k (\mathbf{G})_i^T \rangle w_i [\mathbf{L}]_i^T [\mathbf{R}]_i^T. \end{aligned} \quad (\text{A.15})$$

If the noise in distinct pixels is independent, as assumed, then $\langle (\mathbf{G})_k (\mathbf{G})_i \rangle = \delta_{ki}$, the Kronecker symbol, and so

$$[\mathcal{C}]_j = \sum_k w_k^2 [\mathbf{R}]_k [\mathbf{C}]_k [\mathbf{R}]_k^T, \quad (\text{A.16})$$

which can be computed easily with Eq. A.10.

Developing each term of the matrix, we can see more explicitly how the smoothing mixes the different elements⁶ of the

⁶ For example, \mathcal{C}_{II}^j is the first element of matrix $[\mathcal{C}]_j$ which is being evaluated at the pixel centered on J .

noise covariance matrix:

$$\mathcal{C}_{II}^j = \sum_k w_k^2 \mathbf{C}_{IIk} \quad (\text{A.17})$$

$$\mathcal{C}_{IQ}^j = \sum_k w_k^2 (a \mathbf{C}_{IQk} + b \mathbf{C}_{IUk}) \quad (\text{A.18})$$

$$\mathcal{C}_{IU}^j = \sum_k w_k^2 (-b \mathbf{C}_{IQk} + a \mathbf{C}_{IUk}) \quad (\text{A.19})$$

$$\mathcal{C}_{QQ}^j = \sum_k w_k^2 (a^2 \mathbf{C}_{QQk} + 2ab \mathbf{C}_{QUk} + b^2 \mathbf{C}_{UUk}) \quad (\text{A.20})$$

$$\mathcal{C}_{QU}^j = \sum_k w_k^2 ((a^2 - b^2) \mathbf{C}_{QUk} + ab (\mathbf{C}_{UUk} - \mathbf{C}_{QQk})) \quad (\text{A.21})$$

$$\mathcal{C}_{UU}^j = \sum_k w_k^2 (b^2 \mathbf{C}_{QQk} - 2ab \mathbf{C}_{QUk} + a^2 \mathbf{C}_{UUk}), \quad (\text{A.22})$$

where we note that $a = \cos 2\psi_k^j$ and $b = \sin 2\psi_k^j$ depend on j and k . The mixing of the different elements of the covariance matrix during the smoothing is due not to the smoothing itself, but to the rotation of the polarization frame within the smoothing beam.

A.1.3. Smoothing of the noise covariance matrix with a Monte Carlo approach

For the purpose of this paper, we obtained smoothed covariance matrices using a Monte Carlo approach.

We first generate correlated noise maps (n_I, n_Q, n_U) on I , Q , and U at the resolution of the data using

$$\begin{pmatrix} n_I \\ n_Q \\ n_U \end{pmatrix} = \begin{pmatrix} L_{11} & 0 & 0 \\ L_{12} & L_{22} & 0 \\ L_{13} & L_{23} & L_{33} \end{pmatrix} \times \begin{pmatrix} G_I \\ G_Q \\ G_U \end{pmatrix}. \quad (\text{A.23})$$

where G_I , G_Q , and G_U are Gaussian normalized random vectors and L is the Cholesky decomposition of the covariance matrix $[\mathbf{C}]$ defined in Eq. A.12

The above noise I , Q , and U maps are then smoothed to the requested resolution using the smoothing procedure of the HEALPix package. The noise maps are further resampled using the upgrade procedure of the HEALPix package, so that pixelization respects the Shannon theorem for the desired resolution. The smoothed covariance matrices for each sky pixel are then derived from the statistics of the smoothed noise maps. The Monte Carlo simulations have been performed using 1000 realizations.

Both the analytical and the Monte Carlo approaches have been estimated on the *Planck* data and shown to give equivalent results.

Appendix B: Debiasing methods

Since p is a quadratic function of the observed Stokes parameters (see Eq. 1) it is affected by a positive bias in the presence of noise. The bias becomes dominant at low S/N. Below, we describe a few of the techniques that have been investigated in order to correct for this bias.

B.1. Conventional method (method 1)

This method is the conventional determination (see Planck Collaboration Int. XXIII 2014, for a summary) often used on extinction polarization data. It uses the internal variances provided

with the *Planck* data, which includes the white noise estimate on the intensity (C_{II}) as well as on the Q and U Stokes parameters (C_{QQ} and C_{UU}) and the off-diagonal terms of the noise covariance matrix (C_{IQ}, C_{IU}, C_{QU}).

The debiased p^2 values are computed using

$$p_{\text{db}}^2 = p_{\text{obs}}^2 - \sigma_p^2, \quad (\text{B.1})$$

where σ_p^2 is the variance of p computed from the observed Stokes parameters and the associated variances as follows:

$$\begin{aligned} \sigma_p^2 = & \frac{1}{p^2 I_{\text{obs}}^4} \times (Q^2 C_{QQ} + U^2 C_{UU} + \frac{C_{II}}{I^2} \times (Q^2 + U^2)^2 \\ & + 2QU C_{QU} \\ & - 2Q \frac{(Q^2 + U^2)}{I} C_{IQ} - 2U \frac{(Q^2 + U^2)}{I} C_{IU}). \end{aligned} \quad (\text{B.2})$$

The uncertainty on ψ is given by

$$\sigma_\psi = 28.65^\circ \times \sqrt{\frac{Q^2 C_{UU} + U^2 C_{QQ} - 2QU C_{QU}}{Q^2 C_{QQ} + U^2 C_{UU} + 2QU C_{QU}}} \times \sigma_p, \quad (\text{B.3})$$

where σ_p is the uncertainty on the polarized intensity:

$$\sigma_p = \frac{1}{p^2} (Q^2 C_{QQ} + U^2 C_{UU} + 2QU C_{QU}). \quad (\text{B.4})$$

In the case where I is supposed to be perfectly known, $C_{II} = C_{IQ} = C_{IU} = 0$,

$$\sigma_\psi = 28.65^\circ \times \sqrt{\frac{Q^2 C_{UU} + U^2 C_{QQ} - 2QU C_{QU}}{Q^2 C_{QQ} + U^2 C_{UU} + 2QU C_{QU}}} \times \frac{\sigma_p}{p}. \quad (\text{B.5})$$

It is to be noted that, since it is based on derivatives around the true value of the I , Q , and U parameters, it is only valid in the high S/N regime. The conventional values of uncertainties derived above are compared to the ones obtained using the Bayesian approach in Fig. B.1.

B.2. Time cross-product method (method 2)

This method consists in computing cross products between estimates of Q and U with independent noise properties. In the case of *Planck* HFI, each sky pixel has been observed at least four times and the four independent surveys can be used for this purpose. Another option is to use half-ring maps which have been produced from the first and second halves of each ring. These methods have the disadvantage of using only part of the data, but the advantage of efficiently debiasing the data if the noise is effectively independent, without assumptions about the Q and U uncertainties.

In that case, p_{db}^2 can be computed as

$$p_{\text{db}}^2 = \frac{\sum_{i>j} Q_i Q_j + U_i U_j}{\sum_{i>j} I_i I_j}, \quad (\text{B.6})$$

where the sum is carried out either over independent survey maps or half-ring maps.

The uncertainty of p^2 can in turn be evaluated from the dispersion between pairs

$$\sigma^2(p_{\text{db}}^2) = \frac{\sigma^2(Q^2) + \sigma^2(U^2) + (Q^2 + U^2)/I^2 \sigma^2(I^2)}{I^4}. \quad (\text{B.7})$$

B.3. Bayesian methods (method 3)

We use a method based on the one proposed by Quinn (2012) and extended to the more general case of an arbitrary covariance matrix by Planck Collaboration Int. XXIII (2014). Unlike the conventional method presented in Sect. B.1, this method is in principle accurate at any signal-to-noise ratio. Figure B.1 compares the Bayesian predictions for p and ψ and their uncertainties σ_p and σ_ψ with those obtained from the conventional method (Eq. 1, 2, B.7, and B.6) as predicted from for the *Planck* data at 1° resolution. As can be seen in the figure, the bias on p is generally important even at this low resolution. The conventional uncertainties are accurate only at low uncertainties, as expected since B.7 and B.6 are obtained from Taylor expansion around the true values of the parameters. The difference in the uncertainties is the greatest for σ_ψ as the true value can only reach 52° for purely random orientations.

Appendix C: Tests on $\Delta\psi$ bias

We have performed tests in which we used the *Planck* noise covariance matrices in order to check that the structures we observe in the maps of the polarization angle dispersion function $\Delta\psi$ are not caused by systematic noise bias. One of the tests (called $\Delta\psi = 52^\circ$) consisted of assigning each pixel a random polarization angle ψ . The second one, (called $\Delta\psi = 0^\circ$) consisted of setting ψ to a constant value over the whole sky map, which leads to $\Delta\psi = 0^\circ$ (except near the poles). In that case, changing ψ in the data was done while preserving the value of p and σ_p computed as in Eq. B.2, through the appropriate modification of I , Q , and U . The tests also use the noise covariance of the data, so that the tests are performed with the same sky distribution of the polarization S/N as in the data. This is critical for investigating the spatial distribution of the noise-induced bias on $\Delta\psi$. In both tests, we added correlated noise on I , Q , and U using the actual noise covariance matrix at each pixel, and computed the map of $\Delta\psi$ using Eq. 6 and the same lag value as for the *Planck* data.

Figure C.1 shows the histograms of the $\Delta\psi$ values obtained for these two tests, both for the whole sky and in the mask used in the analysis of the real data. As expected, the $\Delta\psi = 52^\circ$ test histograms peak at the value of $\Delta\psi$ for Gaussian noise only (no signal, $\Delta\psi = 52^\circ$). The corresponding map of $\Delta\psi$ does not exhibit the filamentary structure of the actual data shown in Fig. 11. Similarly, the test histograms of $\Delta\psi$ do not resemble that of the real data shown in Fig. 13. The $\Delta\psi = 0^\circ$ test is important for assessing the amplitude of the noise-induced bias, as Monte Carlo simulations show that assuming a true value of $\Delta\psi_0 = 0^\circ$ maximizes the bias. We therefore use this test as a determination of the upper limit for the bias given the polarization fraction and noise properties of the data. Figure C.1 shows that the histograms of the recovered values peak at $\Delta\psi = 0^\circ$. The histogram is also narrower in the high $\Delta\psi$ S/N region than over the full sky. In the high $\Delta\psi$ S/N mask, 60% of the data points have a noise-induced bias smaller than 1.6° , and 97% have a bias smaller than 9.6° . The maps of the bias computed for this test show a correlation with the map of $\Delta\psi$. However, as shown in Fig. C.1 (lower panel), the effect of the bias is small at high values of $\Delta\psi$ for most pixels and can reach up to 50% for a larger fraction of points at lower $\Delta\psi$ (say below $\Delta\psi = 10^\circ$) values. The map of $\Delta\psi$ with the bias derived using test $\Delta\psi = 0^\circ$ subtracted does not significantly change the structure of the map shown in Fig. 11 and in particular does not explain the filamentary struc-

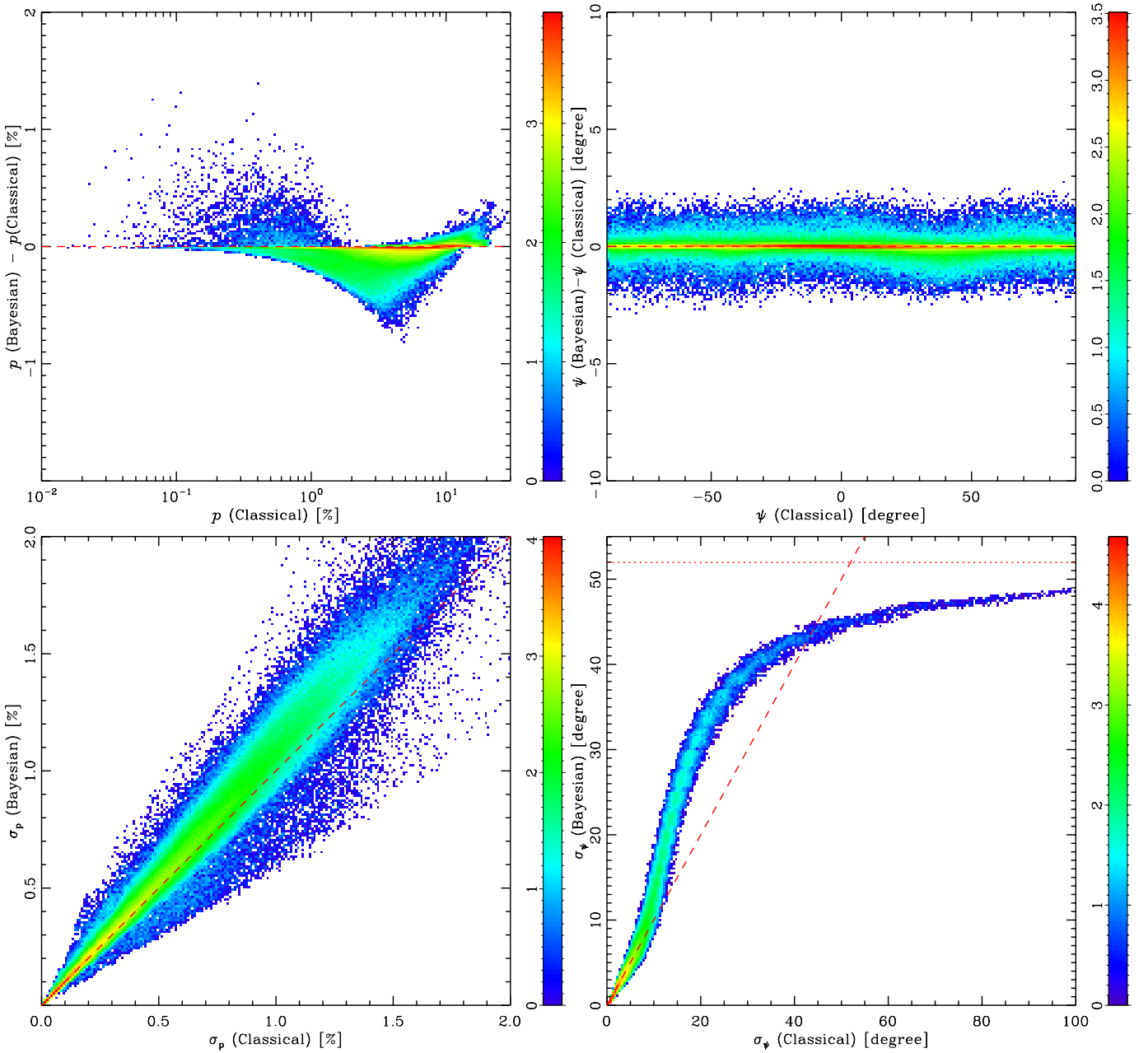


Fig. B.1. *Upper panels:* difference between the conventional and the Bayesian mean posterior estimates of p and ψ as a function of the conventional estimate. *Lower panels:* Bayesian mean posterior estimates of σ_p and σ_ψ as a function of the conventional estimate. The dashed blue lines show where the two methods give the same result. Each plot shows the density of points in log-scale for the *Planck* data at 1° resolution. The dotted line in the lower right plot shows the value for pure noise. The colour scale shows the pixel density on a \log_{10} scale.

tures observed. We note, however, that the noise-induced bias can change the slope of the correlation between $\Delta\psi$ and p .

¹ APC, AstroParticule et Cosmologie, Université Paris Diderot, CNRS/IN2P3, CEA/Irfu, Observatoire de Paris, Sorbonne Paris Cité, 10, rue Alice Domon et Léonie Duquet, 75205 Paris Cedex 13, France

² Aalto University Metsähovi Radio Observatory and Dept of Radio Science and Engineering, P.O. Box 13000, FI-00076 AALTO, Finland

³ African Institute for Mathematical Sciences, 6-8 Melrose Road, Muizenberg, Cape Town, South Africa

⁴ Agenzia Spaziale Italiana Science Data Center, Via del Politecnico snc, 00133, Roma, Italy

⁵ Agenzia Spaziale Italiana, Viale Liegi 26, Roma, Italy

⁶ Astrophysics Group, Cavendish Laboratory, University of Cambridge, J J Thomson Avenue, Cambridge CB3 0HE, U.K.

⁷ Astrophysics & Cosmology Research Unit, School of Mathematics, Statistics & Computer Science, University of KwaZulu-Natal, Westville Campus, Private Bag X54001, Durban 4000, South Africa

⁸ Atacama Large Millimeter/submillimeter Array, ALMA Santiago Central Offices, Alonso de Cordova 3107, Vitacura, Casilla 763 0355, Santiago, Chile

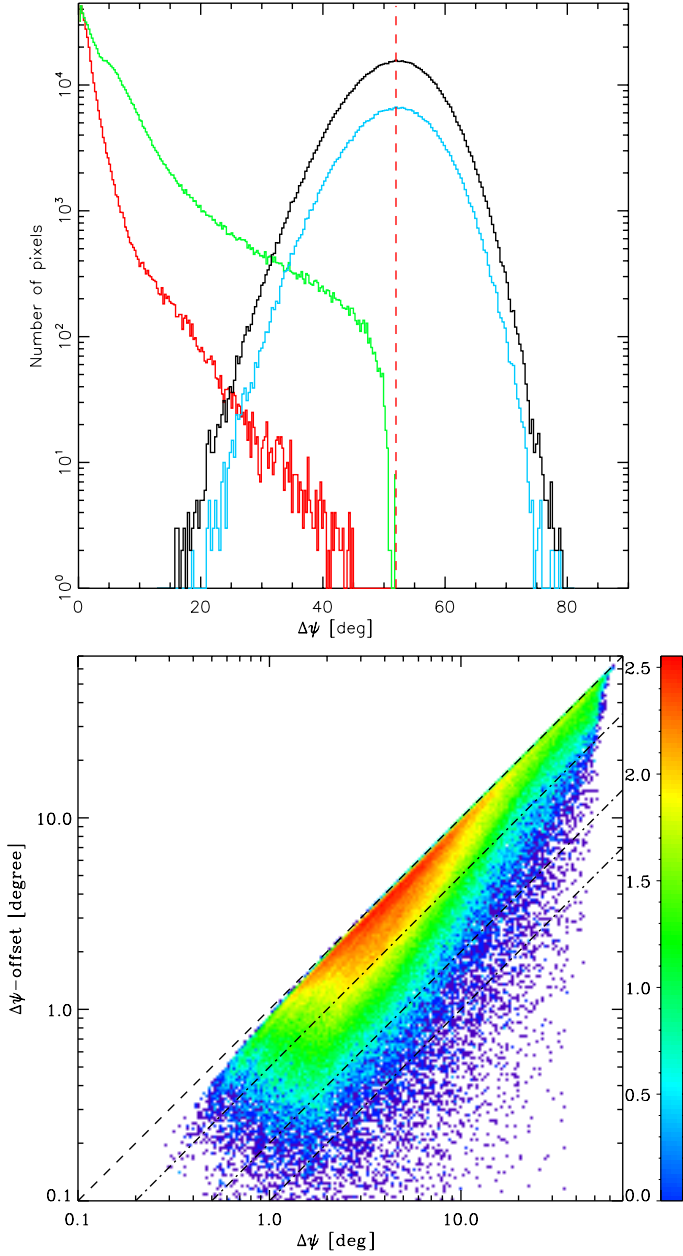


Fig. C.1. *Upper:* histogram of $\Delta\psi$ obtained on simulated data assuming either $\Delta\psi = 0^\circ$ (curves peaking at $\Delta\psi = 0^\circ$) or a random value for $\Delta\psi$ (curves peaking at $\Delta\psi = 52^\circ$) and noise simulated using the actual *Planck* noise covariance matrices. The green and black curves show the histograms and the blue and red curves show histograms where $\Delta\psi/\sigma_\psi > 3$. The vertical dashed line shows $\Delta\psi = 52^\circ$, which is the value for pure random noise on Q and U . *Lower:* distribution of $\Delta\psi$ minus the offset derived from a simulation with $\Delta\psi = 0^\circ$, with respect to $\Delta\psi$, in the region where $\Delta\psi/\sigma_\psi > 3$. Dashed lines show $\Delta\psi = n \times (\Delta\psi - \text{offset})$, with $n=1, 2, 5$, and 10 . The colour scale shows the pixel density on a \log_{10} scale.

- ¹² Centro de Estudios de Física del Cosmos de Aragón (CEFCA), Plaza San Juan, 1, planta 2, E-44001, Teruel, Spain
- ¹³ Computational Cosmology Center, Lawrence Berkeley National Laboratory, Berkeley, California, U.S.A.
- ¹⁴ Consejo Superior de Investigaciones Científicas (CSIC), Madrid, Spain
- ¹⁵ DSM/Irfu/SPP, CEA-Saclay, F-91191 Gif-sur-Yvette Cedex, France
- ¹⁶ DTU Space, National Space Institute, Technical University of Denmark, Elektrovej 327, DK-2800 Kgs. Lyngby, Denmark
- ¹⁷ Département de Physique Théorique, Université de Genève, 24, Quai E. Ansermet, 1211 Genève 4, Switzerland
- ¹⁸ Departamento de Física Fundamental, Facultad de Ciencias, Universidad de Salamanca, 37008 Salamanca, Spain
- ¹⁹ Departamento de Física, Universidad de Oviedo, Avda. Calvo Sotelo s/n, Oviedo, Spain
- ²⁰ Department of Astronomy and Astrophysics, University of Toronto, 50 Saint George Street, Toronto, Ontario, Canada
- ²¹ Department of Astrophysics/IMAPP, Radboud University Nijmegen, P.O. Box 9010, 6500 GL Nijmegen, The Netherlands
- ²² Department of Physics & Astronomy, University of British Columbia, 6224 Agricultural Road, Vancouver, British Columbia, Canada
- ²³ Department of Physics and Astronomy, Dana and David Dornsife College of Letter, Arts and Sciences, University of Southern California, Los Angeles, CA 90089, U.S.A.
- ²⁴ Department of Physics and Astronomy, University College London, London WC1E 6BT, U.K.
- ²⁵ Department of Physics, Florida State University, Keen Physics Building, 77 Chieftan Way, Tallahassee, Florida, U.S.A.
- ²⁶ Department of Physics, Gustaf Hällströmin katu 2a, University of Helsinki, Helsinki, Finland
- ²⁷ Department of Physics, Princeton University, Princeton, New Jersey, U.S.A.
- ²⁸ Department of Physics, University of California, Santa Barbara, California, U.S.A.
- ²⁹ Department of Physics, University of Illinois at Urbana-Champaign, 1110 West Green Street, Urbana, Illinois, U.S.A.
- ³⁰ Dipartimento di Fisica e Astronomia G. Galilei, Università degli Studi di Padova, via Marzolo 8, 35131 Padova, Italy
- ³¹ Dipartimento di Fisica e Scienze della Terra, Università di Ferrara, Via Saragat 1, 44122 Ferrara, Italy
- ³² Dipartimento di Fisica, Università La Sapienza, P. le A. Moro 2, Roma, Italy
- ³³ Dipartimento di Fisica, Università degli Studi di Milano, Via Celoria, 16, Milano, Italy
- ³⁴ Dipartimento di Fisica, Università degli Studi di Trieste, via A. Valerio 2, Trieste, Italy
- ³⁵ Dipartimento di Fisica, Università di Roma Tor Vergata, Via della Ricerca Scientifica, 1, Roma, Italy
- ³⁶ Discovery Center, Niels Bohr Institute, Blegdamsvej 17, Copenhagen, Denmark
- ³⁷ Dpto. Astrofísica, Universidad de La Laguna (ULL), E-38206 La Laguna, Tenerife, Spain
- ³⁸ European Southern Observatory, ESO Vitacura, Alonso de Cordova 3107, Vitacura, Casilla 19001, Santiago, Chile
- ³⁹ European Space Agency, ESAC, Planck Science Office, Camino bajo del Castillo, s/n, Urbanización Villafranca del Castillo, Villanueva de la Cañada, Madrid, Spain
- ⁴⁰ European Space Agency, ESTEC, Keplerlaan 1, 2201 AZ Noordwijk, The Netherlands
- ⁴¹ Helsinki Institute of Physics, Gustaf Hällströmin katu 2, University of Helsinki, Helsinki, Finland
- ⁴² INAF - Osservatorio Astrofisico di Catania, Via S. Sofia 78, Catania, Italy
- ⁴³ INAF - Osservatorio Astronomico di Padova, Vicolo dell'Osservatorio 5, Padova, Italy
- ⁴⁴ INAF - Osservatorio Astronomico di Roma, via di Frascati 33, Monte Porzio Catone, Italy

⁹ CITA, University of Toronto, 60 St. George St., Toronto, ON M5S 3H8, Canada

¹⁰ CNRS, IRAP, 9 Av. colonel Roche, BP 44346, F-31028 Toulouse cedex 4, France

¹¹ California Institute of Technology, Pasadena, California, U.S.A.

- ⁴⁵ INAF - Osservatorio Astronomico di Trieste, Via G.B. Tiepolo 11, Trieste, Italy
- ⁴⁶ INAF/IASF Bologna, Via Gobetti 101, Bologna, Italy
- ⁴⁷ INAF/IASF Milano, Via E. Bassini 15, Milano, Italy
- ⁴⁸ INFN, Sezione di Bologna, Via Irnerio 46, I-40126, Bologna, Italy
- ⁴⁹ INFN, Sezione di Roma 1, Università di Roma Sapienza, Piazzale Aldo Moro 2, 00185, Roma, Italy
- ⁵⁰ INFN/National Institute for Nuclear Physics, Via Valerio 2, I-34127 Trieste, Italy
- ⁵¹ IPAG: Institut de Planétologie et d'Astrophysique de Grenoble, Université Joseph Fourier, Grenoble 1 / CNRS-INSU, UMR 5274, Grenoble, F-38041, France
- ⁵² Imperial College London, Astrophysics group, Blackett Laboratory, Prince Consort Road, London, SW7 2AZ, U.K.
- ⁵³ Infrared Processing and Analysis Center, California Institute of Technology, Pasadena, CA 91125, U.S.A.
- ⁵⁴ Institut d'Astrophysique Spatiale, CNRS (UMR8617) Université Paris-Sud 11, Bâtiment 121, Orsay, France
- ⁵⁵ Institut d'Astrophysique de Paris, CNRS (UMR7095), 98 bis Boulevard Arago, F-75014, Paris, France
- ⁵⁶ Institute for Space Sciences, Bucharest-Magurale, Romania
- ⁵⁷ Institute of Astronomy, University of Cambridge, Madingley Road, Cambridge CB3 0HA, U.K.
- ⁵⁸ Institute of Theoretical Astrophysics, University of Oslo, Blindern, Oslo, Norway
- ⁵⁹ Instituto de Astrofísica de Canarias, C/Vía Láctea s/n, La Laguna, Tenerife, Spain
- ⁶⁰ Instituto de Astronomia, Geofísica e Ciências Atmosféricas, Universidade de São Paulo, São Paulo, SP 05508-090, Brazil
- ⁶¹ Instituto de Física de Cantabria (CSIC-Universidad de Cantabria), Avda. de los Castros s/n, Santander, Spain
- ⁶² Jet Propulsion Laboratory, California Institute of Technology, 4800 Oak Grove Drive, Pasadena, California, U.S.A.
- ⁶³ Jodrell Bank Centre for Astrophysics, Alan Turing Building, School of Physics and Astronomy, The University of Manchester, Oxford Road, Manchester, M13 9PL, U.K.
- ⁶⁴ Kavli Institute for Cosmology Cambridge, Madingley Road, Cambridge, CB3 0HA, U.K.
- ⁶⁵ LAL, Université Paris-Sud, CNRS/IN2P3, Orsay, France
- ⁶⁶ LERMA, CNRS, Observatoire de Paris, 61 Avenue de l'Observatoire, Paris, France
- ⁶⁷ Laboratoire AIM, IRFU/Service d'Astrophysique - CEA/DSM - CNRS - Université Paris Diderot, Bât. 709, CEA-Saclay, F-91191 Gif-sur-Yvette Cedex, France
- ⁶⁸ Laboratoire Traitement et Communication de l'Information, CNRS (UMR 5141) and Télécom ParisTech, 46 rue Barrault F-75634 Paris Cedex 13, France
- ⁶⁹ Laboratoire de Physique Subatomique et de Cosmologie, Université Joseph Fourier Grenoble I, CNRS/IN2P3, Institut National Polytechnique de Grenoble, 53 rue des Martyrs, 38026 Grenoble cedex, France
- ⁷⁰ Laboratoire de Physique Théorique, Université Paris-Sud 11 & CNRS, Bâtiment 210, 91405 Orsay, France
- ⁷¹ Lawrence Berkeley National Laboratory, Berkeley, California, U.S.A.
- ⁷² Max-Planck-Institut für Astrophysik, Karl-Schwarzschild-Str. 1, 85741 Garching, Germany
- ⁷³ National University of Ireland, Department of Experimental Physics, Maynooth, Co. Kildare, Ireland
- ⁷⁴ Niels Bohr Institute, Blegdamsvej 17, Copenhagen, Denmark
- ⁷⁵ Observational Cosmology, Mail Stop 367-17, California Institute of Technology, Pasadena, CA, 91125, U.S.A.
- ⁷⁶ Optical Science Laboratory, University College London, Gower Street, London, U.K.
- ⁷⁷ SISSA, Astrophysics Sector, via Bonomea 265, 34136, Trieste, Italy
- ⁷⁸ School of Physics and Astronomy, Cardiff University, Queens Buildings, The Parade, Cardiff, CF24 3AA, U.K.
- ⁷⁹ Space Sciences Laboratory, University of California, Berkeley, California, U.S.A.
- ⁸⁰ Special Astrophysical Observatory, Russian Academy of Sciences, Nizhnij Arkhyz, Zelenchukskiy region, Karachai-Cherkessian Republic, 369167, Russia
- ⁸¹ Sub-Department of Astrophysics, University of Oxford, Keble Road, Oxford OX1 3RH, U.K.
- ⁸² UPMC Univ Paris 06, UMR7095, 98 bis Boulevard Arago, F-75014, Paris, France
- ⁸³ Université de Toulouse, UPS-OMP, IRAP, F-31028 Toulouse cedex 4, France
- ⁸⁴ Universities Space Research Association, Stratospheric Observatory for Infrared Astronomy, MS 232-11, Moffett Field, CA 94035, U.S.A.
- ⁸⁵ University of Granada, Departamento de Física Teórica y del Cosmos, Facultad de Ciencias, Granada, Spain
- ⁸⁶ University of Granada, Instituto Carlos I de Física Teórica y Computacional, Granada, Spain
- ⁸⁷ Warsaw University Observatory, Aleje Ujazdowskie 4, 00-478 Warszawa, Poland